Multiband diffusion-weighted MRI of the eye and orbit free of geometric distortions using a RARE-EPI hybrid

Paul K., Huelnhagen T., Oberacker E., Wenz D., Kuehne A., Waiczies H., Schmitter S., Stachs O., Niendorf T.

This is the final version of the accepted manuscript, which was published in final edited form in:

NMR in Biomedicine
2018 MAR; 31(3): e3872
2018 JAN 09 (first published online)
doi: 10.1002/nbm.3872

Publisher: Wiley

Multiband Diffusion-Weighted MRI of the Eye and Orbit Free of Geometric Distortions Using a RARE-EPI Hybrid

Katharina Paul[1]; Till Huelnhagen[1]; Eva Oberacker[1]; Daniel Wenz[1]; André Kuehne[2]; Helmar Waiczies[2]; Sebastian Schmitter[3]; Oliver Stachs[4]; Thoralf Niendorf[1,5]

[1] Berlin Ultrahigh Field Facility (B.U.F.F.), Max Delbrueck Center for Molecular Medicine in the Helmholtz Association, Berlin Germany
[2] MRI.TOOLS GmbH, Berlin, Germany
[3] Medical Physics and Metrological Information Technology, Physikalisch-Technische Bundesanstalt, Berlin, Germany
[4] Department of Ophthalmology, University of Rostock, Rostock, Germany
[5] Experimental and Clinical Research Center (ECRC), a joint cooperation between the Charité Medical Faculty and the Max Delbrueck Center for Molecular Medicine in the Helmholtz Association, Berlin, Germany

Correspondence to: Prof. Dr. Thoralf Niendorf
Berlin Ultrahigh Field Facility (B.U.F.F.)
Max-Delbrueck-Center for Molecular Medicine
Robert-Roessle-Strasse 10
13125 Berlin
Germany

phone: +49 30 9406 4505
fax: +49 30 9406 49178
e-mail: thoralf.niendorf@mdc-berlin.de

word count: maint text ≈ 5100

LIST OF ABBREVIATIONS

ADC	apparent diffusion coefficient
BWTP	bandwidth time product
CAIPIRINHA	Controlled Aliasing in Parallel Imaging Results in Higher Acceleration
CAT	combined acquisition technique
CPMG	Carr Purcell Meiboom Gill
DWI	diffusion-weighted imaging
EPI	echo planar imaging
ETL	echo train length
FLASH	fast low angle shot
FSE	fast spin echo
GRAPPA	GeneRalized Autocalibrating Partial Parallel Acquisition
MB	multiband
MRI	magnetic resonance imaging
ms-RARE	multi-shot rapid acquisition with relaxation enhancement
MUSE	multiplexed sensitivity encoding
PINS	power independent number of slices
PROPELLER	periodically rotated overlapping parallel lines with enhanced reconstruction
PSF	point spread function
RARE	Rapid acquisition with relaxation enhancement
RF	radiofrequency
ROI	region of interest
rs-EPI	readout-segment echo planar imaging
SG	slice GRAPPA
ss-EPI	single-shot echo planar imaging
SSGR	slice selection gradient reversal

ABSTRACT

Diffusion-weighted imaging (DWI) provides information about tissue microstructure. Single-shot echo planar EPI is the most common technique for DWI applications in the brain but is prone to geometric distortions and signal voids. Rapid Acquisition with Relaxation Enhancement imaging (RARE, also known as FSE) presents a valuable alternative for DWI with high anatomic accuracy. This work proposes a multi-shot diffusion-weighted RARE-EPI hybrid pulse sequence, joining the anatomical integrity of RARE with the imaging speed and radiofrequency (RF) power deposition advantage of EPI. Anatomical integrity of RARE-EPI was demonstrated and quantified by center of gravity analysis, both for morphological images and diffusion-weighted acquisitions in phantom and in-vivo experiments at 3.0 T and at 7.0 T. The results indicate that half of the RARE echoes in the echo train can be replaced by EPI echoes while maintaining anatomical accuracy. The reduced RF power deposition of RARE-EPI enabled multiband RF pulses facilitating simultaneous multi-slice imaging. This study shows that diffusion-weighted RARE-EPI has the capability to acquire high fidelity, distortion-free images of the eye and the orbit. It is shown that RARE-EPI maintains the immunity to B_0 inhomogeneities reported for RARE imaging. This benefit can be exploited for the assessment of ocular masses and pathologic changes of the eye and the orbit.

INTRODUCTION

Magnetic resonance imaging (MRI) of the eye and the orbit is an emerging application that is increasingly used in ophthalmology. The benefits of ocular MRI for studying the spatial arrangements [1-4], structure and function of the eye [5,6], for assessing ophthalmological disorders [7-14] and for guiding diagnosis and treatment of ophthalmological diseases [2,14-20] are of proven value.

Diffusion-weighted imaging (DWI) is an approach that provides information about tissue microstructure in-vivo allowing tissue characterization [21,22]. It has been shown that ophthalmic DWI affords the detection of subchoroidal and subretinal abscesses [23,24]. Also, the involvement of extraocular muscles in thyroid eye disease can be examined with ocular DWI [25] and solitary orbital tumors can be identified with DWI [26]. Furthermore, DWI benefits the differentiation between ocular tumors and retinal detachment [8,10,27]and it supports the diagnosis of ischemic optic neuropathy and optic neuritis [28-30]. It also has been shown that DWI is sensitive to changes in the vitreous humor during aging [31]. Recently, ophthalmic DWI has been applied to monitor proton beam therapy of uveal melanoma [32,33]. This wide range of applications demonstrates the clinical value of ocular DWI.

Single-shot echo planar imaging (ss-EPI) is the most widely applied technique for rapid in-vivo DWI. It offers excellent acquisition speed, reduces sensitivity to bulk motion and provides reasonable spatial resolution. Notwithstanding these benefits, EPI is prone to magnetic susceptibility variations that result in signal voids and image distortion. These effects increase with magnetic field strength and are pronounced in regions with high deviations of the main magnetic field (B_0). Thus, DWI of cranial regions proximal to air filled cavities, sinuses or in close vicinity to skin/muscle/bone/brain boundaries is particularly susceptible to geometric distortions. This constraint constitutes a severe challenge for diffusion-weighted EPI of the eye and orbit [27,34].

To address this constraint, multi-shot approaches including interleaved EPI, periodically rotated overlapping parallel lines with enhanced reconstruction (PROPELLER) strategies [35] and read-out segmented *k*-space data acquisition schemes [36] have been proposed to reduce geometric distortion and to improve the anatomic accuracy of EPI. Readout segmented EPI (rs-EPI) supports DWI of the brain at 3.0 and at 7.0 T with largely reduced susceptibility artifacts [37,38], but was reported to be prone to severe distortions for DWI of the eye and orbit [34,39]. Recent neuroimaging work demonstrated the feasibility of high spatial resolution diffusion imaging of the human cerebrum and brainstem using a hybrid spin-warp and echo-planar point spread function (PSF) encoded strategy [40].

Fast spin-echo (FSE) or Rapid Acquisition with Relaxation Enhancement (RARE) techniques present a valuable alternative for DWI of the eye and orbit providing high anatomic accuracy [41-43]. Diffusion-weighted single-shot RARE has been applied for the assessment of retinoblastoma [8], while

segmented diffusion-weighted RARE (ms-RARE) has been shown to be suitable for the detection of intraocular masses with ample diffusion contrast versus the subretinal hemorrhage and the vitreous body [39].

RARE uses a train of refocusing pulses, resulting in an imaging speed and RF power deposition handicap over EPI. To address these constraints, Combined Acquisition Techniques (CAT) [44] have been applied to boost imaging speed and to reduce RF power deposition by using a modular hybrid approach that integrates a minimum of two imaging strategies. CAT variants include FLASH-EPI, FLASH-BURST and RARE-EPI hybrids that have been implemented for cardiac, abdominal and neuroimaging [45-47]. A RARE-EPI hybrid is conceptually appealing for the pursuit of ocular MRI at (ultra)high fields due to the anatomical integrity of RARE in conjunction with the imaging speed and RF power deposition advantage of EPI. It holds the promise to further improve the usability and applicability of our previously reported diffusion-weighted ms-RARE variant [39]. Due to the reduced power deposition, RARE-EPI offers the potential for increasing the spatial coverage by simultaneous multi-slice imaging [48] techniques, which are inherently RF power demanding.

Recognizing the challenges of DWI free of geometric distortion and realizing the opportunities for ophthalmic imaging discovery along with the advances in (ultra)high field MRI, this work examines the applicability of diffusion-weighted RARE-EPI for anatomically accurate DWI of the eye and the orbit at 3.0 T and 7.0 T. To meet this goal we extended our previous work and implemented a multi-shot RARE-EPI variant and incorporated diffusion-sensitization preparation (DW-RARE-EPI). A navigator echo is added for shot-to-shot bulk motion induced phase error estimation and correction, and simultaneous multi-slice imaging is integrated for acceleration. The suitability of DW-RARE-EPI for geometric distortion free imaging is carefully examined in phantom experiments and benchmarked against single shot EPI, read-out segmented EPI and multi-shot RARE. The clinical feasibility of DW-RARE-EPI for imaging of the eye and the orbit free of geometric distortions is demonstrated in a feasibility study in healthy subjects at 3.0 T and 7.0 T as a mandatory precursor to broader clinical studies.

METHODS

Diffusion-Weighted Imaging Techniques

The diffusion-weighted RARE-EPI combined acquisition (DW-RARE-EPI) variant is shown schematically in Figure 1a including diffusion sensitization, phase correction for motion compensation and the imaging module [39,49]. In the RARE-EPI hybrid [(1-λ)·ETL] RARE echoes were replaced by EPI echoes (ETL = echo train length) where λ (0≤λ≤1) defines the fraction of echoes within the echo train covered by the RARE module [44]. The dephasing gradient in frequency encoding direction is imbalanced to separate the echo into two groups [50]. This approach is employed to avoid destructive interferences between even and odd echoes which result from violation of the Carr-Purcell-Meiboom-Gill (CPMG) condition due to the diffusion preparation. Unipolar diffusion sensitization gradients were placed along the phase encoding direction and played out prior and after the first refocusing pulse. The first two echoes were acquired without phase encoding to enable 1D navigator phase correction to compensate for rigid body motion artifacts induced by unknown phase shifts generated by the diffusion sensitization preparation module. The temporal position of RARE and EPI echoes may differ due to system imperfections, eddy currents and main magnetic field inhomogeneities, possibly resulting in image artifacts. Therefore, one dummy excitation without phase encoding gradients turned on was acquired prior to the actual data acquisition as a reference to non-linearly correct the temporal position and phase of RARE and EPI echoes that are combined within one k-space [51].

To maintain geometrical integrity of RARE-EPI the center of k-space was filled with data from the RARE echo train while a train of gradient recalled echoes was used to sample the periphery of k-space. Data were acquired center-out in k-space together with a minimal TE for diffusion-weighted acquisitions (Figure 1b). In case of T_2 weighted acquisitions a linear phase encoding scheme in conjunction with partial Fourier sampling was applied to allow for larger TE values while ensuring an ample share of RARE echoes in the center of k-space (Figure 1c).

For comparison, three alternative diffusion-weighted pulse techniques were employed: (i) multi-shot RARE (ms-RARE) [39] that was recently proposed for diffusion-weighted imaging free of geometric distortions, which is identical to DW-RARE-EPI with λ = 1, (ii) single-shot EPI (ss-EPI) as the clinical standard for DWI and (iii) readout-segmented EPI (rs-EPI) as a sophisticated EPI variant [37,38].

Magnetic Resonance Hardware

Phantom experiments and in-vivo studies were performed on a 3.0 T whole body MR system (Magnetom Verio, Siemens, Erlangen, Germany; maximum gradient strength 40 mT/m, maximum slew rate 200 mT/m/ms) and on a 7.0 T whole body MR system (Magnetom, Siemens, Erlangen,

Germany; maximum gradient strength 38 mT/m, maximum slew rate 170 mT/m/ms). At 3.0 T a body volume RF coil was used for signal transmission and a 32-channel head RF coil (Siemens, Erlangen, Germany) was applied for signal reception. A dedicated six-element transceiver RF coil array consisting of loop elements was employed for in-vivo ophthalmic MRI at 7.0 T [13] (MRI.TOOLS GmbH, Berlin, Germany) utilizing the parallel transmission system with a fixed phase setting. For phantom and brain MRI at 7.0 T, a 24-element RF coil array (Nova Medical, Wilmington, USA) was used, which is equipped with a quadrature RF volume resonator used for transmission. Figure 2 shows photographs of the applied RF coil setups.

Phantom Experiments

To examine the geometric integrity of DW-RARE-EPI, a cylindrical structure phantom was used (Siemens Multipurpose-Phantom E, diameter = 18 cm, height = 14 cm). A transaxial slice covering five cylinders (diameter = 3.5 cm) containing different concentrations of $MnCl_2$ in distilled water ($MnCl_2$ per 1000g H_2O dist.: 10 mg, 20 mg, 40 mg, 70 mg, 120 mg) was chosen for imaging. Relaxation properties are summarized in Table 1. Morphological images and diffusion-weighted data were acquired at 3.0 T and at 7.0 T for (i) ms-RARE ($\lambda = 1$), (ii) DW-RARE-EPI using $\lambda = 0.7$, $\lambda = 0.6$ and $\lambda = 0.5$ together with an ETL of 16, (iii) ss-EPI (GRAPPA [52] R = 3) and (iv) rs-EPI (nine readout segments, GRAPPA R =2). For each technique the shortest TE possible was set to maximize the signal. Eight b-values (b = 50 s/mm^2 plus b = 100 s/mm^2 to b = 700 s/mm^2 with an increment of b = 100 s/mm^2) were used to acquire sets of diffusion-weighted data. A Fast Low Angle Shot (FLASH) acquisition exhibiting identical geometric parameters was used as a reference. The nominal flip angle of the refocusing pulses α was set to 180° in all imaging protocols. Table 2 provides the full compilation of imaging parameters used for the experiments in this work.

Ethics Statement

In-vivo feasibility studies at 3.0 T and 7.0 T were approved by the local ethical committee (registration number DE/CA73/5550/09, Landesamt für Arbeitsschutz, Gesundheitsschutz und technische Sicherheit, Berlin, Germany). Informed written consent was obtained from each volunteer prior to the study in compliance with the local institutional review board guidelines.

Feasibility Study in Healthy Volunteers

A feasibility study in healthy volunteers (n = 8 (3 male), mean age = (31.6 ± 8.0) years, mean BMI = (22.9 ± 2.7) kg/m^2) was performed at 3.0 T and at 7.0 T. The experiments included anatomical

brain images, apparent diffusion coefficient (ADC) mapping of the eyes, morphological brain multiband imaging and multiband ADC mapping of the eyes.

In-vivo anatomical brain images were acquired at 3.0 T and at 7.0 T in healthy volunteers to demonstrate the comparability of RARE-EPI with conventional RARE. For the RARE-EPI hybrid an ETL of 16 was chosen, and λ = 0.6 (10 RARE echoes, 6 EPI echoes) and λ = 0.5 (8 RARE echoes, 8 EPI echoes) were applied. Slice selection gradient reversal (SSGR) was applied for fat suppression [53].

To elucidate the immunity of DW-RARE-EPI, ms-RARE (λ = 1), ss-EPI and rs-EPI to geometric distortions, ADC mapping of the eyes was performed at 3.0 T. Six b-values (b = 50 s/mm^2 plus b = 100 s/mm^2 to b = 500 s/mm^2 with an increment of b = 100s/mm^2) were employed to generate series of diffusion-weighted data. A T_2-weighted RARE image exhibiting identical geometric parameters was acquired for anatomical reference.

To demonstrate the applicability of DW-RARE-EPI at ultrahigh magnetic field strengths, ADC mapping of the eyes was performed at 7.0 T using ms-RARE (λ = 1) and DW-RARE-EPI. Six b-values (b = 50 s/mm^2 plus b = 100 s/mm^2 to b = 500 s/mm^2 with an increment of b = 100s/mm^2) were employed to generate series of diffusion-weighted data. Phase encoding was set anterior-posterior at 7.0 T enabled by the coil's low sensitivity in the posterior brain and thus allowing the acquisition of a reduced number of phase encoding lines to shorten the acquisition time.

Multiband (MB) imaging with a MB factor of 2 was performed at 3.0 T to increase the spatial coverage. Two Hanning filtered SINC pulses with a bandwidth-time-product (BWTP) of 1.15 were added. The pulse duration was 0.8 ms for the excitation pulse and 1.6 ms for the refocusing pulses. An additional phase increment of 180° was added for every other k-space line for the second slice to facilitate CAIPIRINHA (Controlled Aliasing in Parallel Imaging Results in Higher Acceleration) encoding along the slice direction [54]. A constant phase of 90° was applied for one slice to reduce the peak power of the multiband RF pulse [55]. Morphological and diffusion-weighted images were acquired for the cylindrical structure phantom and for two brain slices separated by a 1 cm gap and covering the eyes were acquired as proof of principle using RARE and RARE-EPI (λ = 0.6) in three different volunteers. The range of applied b-values for multiband ADC mapping was identical to the in-vivo measurements described above. To explicate the immunity of multiband DW-RARE-EPI to geometric distortions, ADC mapping was performed in comparison to ms-RARE (λ = 1), ss-EPI and rs-EPI.

Data Analysis

To visualize the extent of geometric distortions, contours around the cylindrical structures in the phantom were defined in the FLASH reference image and copied to the data obtained with ms-RARE, RARE-EPI, ss-EPI and rs-EPI. Center of gravity analysis was performed to quantify

geometric distortions that occur primarily asymmetrically in phase encoding direction (MATLAB, The Mathworks, Natick, MA). For this purpose, the areas within the contours were determined and the center of gravity was calculated for each structure. The deviation of the center of gravity (in pixels) was calculated with respect to the FLASH reference image. All displacements obtained were averaged over all structures for each imaging approach.

Edge sharpness was assessed by line profile analysis. For this purpose a profile covering the boundary between the vitreous humor and the sclera of the left eye and another profile covering the edge of the posterior skull area were chosen for the assay. The signal intensity SI along the profile was fitted to a sigmoid function described by

$$SI(x; c_0, c_1, c_2, s) = \frac{c_1}{1 + 10^{s(c_0 - x)}} + c_2$$

where x as the independent variable is the distance, c_0 is the center location, c_1 describes the vertical range and c_2 determines the vertical offset while s defines the sharpness of the sigmoid. A least-squares curve fit was chosen and the parameter s provides a measure for edge sharpness [56].

ADC maps were generated by fitting a linear function to the data points obtained for a series of b-values after taking the logarithm of the signal intensity. The outer contour of the phantom was used to mask the ADC maps to only show values within the phantom. In-vivo ADC maps were masked using the boundaries of the eyeballs and superimposed to the anatomical reference images.

Unaliasing of multiband data was performed using a slice GRAPPA (SG) algorithm [57]. Reconstruction kernels (size: 5 x 5) were calibrated using single band RARE data acquired with a reduced matrix size of 128 x 128 to accelerate the acquisition of the calibration scan. These calibration data were applied for the reconstruction of all acquired multiband data with varying values of λ and for all b-values. To quantify the quality of the slice separation signal leakage $L_{i\to j}$ (i,j = 1,2) from slice i into slice j (ideally 0%) as well as the passing signal $L_{i\to i}$ (ideally 100%) was determined by applying the SG reconstruction to the single-band data of slice i [58]. The obtained leakage signal was normalized by the mean signal magnitude of the single-band image determined within a region of interest (ROI) covering the vitreous humor in the left eye. The 99th percentile of $L_{i\to j}$ indicated by $L_{i\to j}^{99\%}$ was calculated as a measure for slice separation quality [59].

RESULTS

Phantom Experiments

Figure 3 summarizes the results obtained for phantom imaging using ms-RARE, DW-RARE-EPI, ss-EPI and rs-EPI at 3.0 T and 7.0 T. Morphological images (Figure 3b) are shown as well as masked ADC maps (Figure 3c) and difference maps with respect to the FLASH reference image (Figure 3d). Using a factor λ of 0.7 (11 RARE echoes, 5 EPI echoes) and 0.6 (10 RARE echoes, 6 EPI echoes) generates results exhibiting image quality comparable to conventional RARE imaging (λ = 1). Decreasing λ to 0.5 (8 RARE echoes, 8 EPI echoes) causes minor artifacts in regions with high signal intensity and strong signal intensity gradients like the phantom boundary both at 3.0 T and at 7.0 T. The artifact is caused by a jump in signal intensity in k-space at the position of the change between RARE and EPI echoes. For lower values of λ the transition moves closer to the center of k-space meaning that the effect on image quality is more pronounced.

Frequency offsets across the measured slices were ΔB_0 = 29.2 Hz at 3.0 T and 56.6 Hz at 7.0 T (Figure 3a). A center of gravity examination of the phantom images revealed minor distortions for RARE of (1.66 ± 0.18) pixels for 3.0 T and (0.41 ± 0.14) pixels at 7.0 T with respect to the FLASH reference, which can be attributed to differences in the PSF of the two imaging techniques. The displacement in the center of gravity versus the FLASH reference was severely increased for ss-EPI (d = (3.00 ± 1.56) pixels at 3.0 T and d = (6.36 ± 4.08) pixels at 7.0 T). For the structure phantom used, rs-EPI yielded minor geometric distortions (d = (2.36 ± 0.17) pixels at 3.0 T and d = (1.87 ± 1.10) pixels at 7.0 T). Decreasing the factor λ in RARE-EPI, i.e. increasing the share of EPI echoes in the echo train, did not impede geometric integrity, meaning that no increase in deviations from the anatomic FLASH reference was observed.

PSF measurement and analysis have been performed to quantify the extent of image blurring induced by replacing RARE by EPI echoes. The measurements revealed a 13% increase in the full width half maximum of the PSF when replacing half of the RARE echo train by EPI echoes (λ = 0.5). Figure 4 summarizes the results of the PSF analysis for RARE (λ = 1) and RARE-EPI with λ = 0.7, λ = 0.6 and λ = 0.5.

The ADC maps in Figure 3c demonstrate the feasibility of diffusion-weighted RARE-EPI. The ADC maps calculated from diffusion-weighted data series acquired with λ = 0.7, λ = 0.6 and λ = 0.5 showed no decrease in image quality due to the increasing replacement of RARE echoes by EPI echoes. Mean ADC values (± standard deviation) at room temperature determined in an ROI placed within the distilled water compartment in the phantom are summarized in Table 3.

The reduction of RF energy per TR with increasing factor λ was assessed using the integral of the squared RF pulses as a metric. Using λ = 0.5 reduces the administered RF power deposition by 36% assuming an ETL of 16 plus 3 dummy RF pulses.

Volunteer Feasibility Study

Figure 5 shows anatomical data for brain slices including the eyes comparing conventional RARE (λ = 1) with RARE-EPI (λ = 0.6 and λ = 0.5) acquired at 3.0 T and at 7.0 T. Image quality and contrast are maintained for RARE-EPI which manifests itself in the visibility of subtle anatomical structures as demonstrated in the zoomed views of Figure 5. To keep minor artifacts at boundaries with high signal intensity gradients and in regions with high signal intensity like the vitreous humor at a minimum, the acquisitions were performed in conjunction with fat suppression. Figure 5c demonstrates the effect of the applied phase correction algorithm and how imaging artifacts generated by differences in phase and temporal position between RARE and EPI echoes are avoided. Additionally, one image where EPI echo lines were filled by zeros in k-space is shown. Replacing the RARE readout in part of the k-space with EPI echoes results in the desired spatial resolution without introducing blurring.

To illustrate the immunity of DW-RARE-EPI to geometric distortions in comparison to diffusion-weighted RARE, ss-EPI and rs-EPI (Figure 6a), ADC maps acquired at 3.0 T are presented in Figure 6b,c. The overlay in Figure 6c shows the superposition of the masked ADC map and the anatomical reference image deduced from diffusion-weighted RARE (Figure 6a). Mean ADC values within the vitreous humor in the shown exemplary volunteer were $ADC_{RARE} = (2.73 \pm 0.19) \cdot 10^{-3}$ mm^2/s, $ADC_{DW\text{-}RARE\text{-}EPI} = (2.77 \pm 0.20) \cdot 10^{-3}$ mm^2/s, $ADC_{ss\text{-}EPI} = (2.86 \pm 0.33) \cdot 10^{-3}$ mm^2/s and $ADC_{rs\text{-}EPI} = (3.19 \pm 0.81) \cdot 10^{-3}$ mm^2/s. These apparent diffusion coefficients compare well with ADCs previously reported for the vitreous body using diffusion-weighted ss-EPI of the eye at 1.5 T [27,31].

A closer examination of the anatomic integrity revealed severe geometric distortions of both eyeballs for ss-EPI (deviation d = (7.96 ± 2.57) pixels) while rs-EPI showed minor distortions (d = (1.73 ± 0.20) pixels) as demonstrated in Figure 6d. DW-RARE-EPI (λ=0.5) exhibited anatomical integrity comparable to RARE based ADC mapping, manifesting itself in a deviation of (1.12 ± 0.02) pixels of the center of gravity. No geometric distortions and no other imaging artifacts related to the replacement of RARE echoes by EPI echoes were detected for DW-RARE-EPI (λ = 0.5) as indicated by the match between the ADC maps superimposed to anatomic reference images. To demonstrate the feasibility of DW-RARE-EPI with reduced voxel sizes ADC maps exhibiting a spatial resolution of (0.9 x 0.9 x 3.0) mm^3 are shown in Figure 6e.

When benchmarking the apparent diffusion coefficients of the eyes derived from DW-RARE-EPI with those from RARE, a linear relationship between $ADC_{RARE\ (\lambda = 1)}$ and $ADC_{RARE\text{-}EPI\ (\lambda = 0.5)}$ was found, which can be described by $y = 1.01 \cdot x$ with a root mean square error of $2.73 \cdot 10^{-4}$ (Figure 6f). This finding confirms the results obtained in the phantom assessment and endorses the validity of the diffusion-weighting within in DW-RARE-EPI. The Bland-Altman plot in Figure 6g underpins the close match between $ADC_{RARE\ (\lambda = 1)}$ and $ADC_{RARE\text{-}EPI\ (\lambda = 0.5)}$ with a mean difference ($ADC_{RARE\ (\lambda = 1)}$ - $ADC_{RARE\text{-}EPI\ (\lambda = 0.5)}$) of $-3.5 \cdot 10^{-5}$ mm^2/s and a +/-1.96 standard deviation of $4.98/-5.68 \cdot 10^{-4}$ mm^2/s.

Figure 7 shows diffusion-weighted RARE-EPI and ms-RARE images obtained at 7.0 T with b-values of 50 s/mm^2 and 500 s/mm^2 as well as corresponding ADC maps. A quantitative analysis revealed a mean ADC (± standard deviation) in the vitreous humor of $(2.80 \pm 0.26) \cdot 10^{-3}$ mm^2/s for ms-RARE and $(2.88 \pm 0.23) \cdot 10^{-3}$ mm^2/s for DW-RARE-EPI ($\lambda = 0.5$). These values agree with ADC values determined at 3.0 T and with literature values [27,31]. Ghosts induced by the sharp eye ball boundary can be seen in the anatomical image acquired with conventional RARE ($\lambda = 1$) and are pronounced in the RARE-EPI ($\lambda = 0.5$) acquisition. This artifact can be attributed to the strong gradient in signal intensity due to the high signal intensity level within in the vitreous humor. In diffusion-weighted images this effect is offset due to lower signal intensity levels. The difference in center of gravity of RARE-EPI in comparison to ms-RARE was determined to be 0.14 pixel. Taking this result together with the phantom analysis into account demonstrates that no geometric distortions are induced by replacing RARE echoes within the echo train by EPI echoes at 7.0 T.

Figure 8 shows the results of the edge sharpness and mean ADC value analysis performed for all subjects included in the feasibility study. For the edge sharpness using the eye boundary the mean s-value is reduced from 0.83 to 0.67 when reducing λ from 1.0 to 0.6 (Figure 8a). An unpaired t-test after a positive Kolmogorov-Smirnov normality test revealed a p-value of 0.21 meaning that this difference is non-significant. When using the skull boundary the mean s-value for $\lambda = 1$ is 0.87 and 0.86 for $\lambda = 0.6$ (Figure 8b). The t-test revealed a non-significant p-value of 0.95. Mean ADC values for RARE and RARE-EPI ($\lambda = 0.6$) match very well as demonstrated in Figure 8c and reflect literature values reported before[31].

Figure 9 summarizes the results of the multiband DWI phantom study. MB RARE, MB RARE-EPI with $\lambda = 0.6$, ss-EPI and rs-EPI are compared in terms of geometric distortions. The displacement of the center of gravity was determined with respect to the FLASH reference. ss-EPI and rs-EPI showed increased geometric distortions in comparison to RARE and RARE-EPI. The distortions for slice 1 and slice 2 were in the same range for all approaches. Also, the ADC values determined in the distilled water compartment of the phantom were comparable for both slices and match with the results obtained from the single slice study presented in Figure 3.

The results obtained for morphological simultaneous multi-slice RARE-EPI imaging are summarized in Figure 10. The location of the two selected slices displaced by 1 cm is illustrated in Figure 10a. Aliased and un-aliased images derived from multiband RARE, RARE-EPI (λ = 0.6) and RARE-EPI (λ = 0.5) are shown in Figure 10b together with normalized leakage values $L_{i\rightarrow j}$ (Figure 10c). The unaliased MB images for slice 1 and slice 2 demonstrate successful slice separation for the applied range of λ-values. The quantitative analysis of signal leakage from slice 1 into slice 2 and vice versa revealed $L_{i\rightarrow j}^{99\%}$ values of 8.5%/8.3% ($L_{1\rightarrow 2}^{99\%}/L_{2\rightarrow 1}^{99\%}$) for λ = 1, 7.5%/7.5% for λ = 0.7 and 7.9%/8.1% for λ = 0.6.

In analogy to the single band data presented in Figure 6, Figure 11 illustrates the immunity of multiband DW-RARE-EPI ADC mapping to geometric distortions. This manifests itself in the minor displacement of the center of gravity of both eye balls of less than one pixel for RARE-EPI with respect to ms-RARE. Contrary to that, ss-EPI and rs-EPI showed severe geometric distortions with displacements in the range of one magnitude higher than for RARE-EPI.

Diffusion-weighted simultaneous multi-slice RARE-EPI (λ = 0.6) data and the corresponding ADC maps are displayed in Figure 12 for a healthy volunteer and a subject with an arachnoidal cyst as proof of principle. Successful slice separation was achieved for the complete range of applied b-values using a non-diffusion-weighted calibration data set with half resolution compared to the multiband data. The mean ADC value within the arachnoidal cyst was approximately 3 fold higher with an ADC value of $(2.88 \pm 0.45) \cdot 10^{-3}$ mm^2/s compared to adjacent white and gray matter brain tissues exhibiting ADCs of $(0.92 \pm 0.24) \cdot 10^{-3}$ mm^2/s (Figure 12b). The benign and asymptomatic cyst containing cerebrospinal fluid and being located in the left temporal lobe is sharply delineated from the surrounding tissue. No geometric distortions were observed despite the prefrontal location and the close proximity to the nasal and frontal sinuses allowing an anatomically accurate assessment of the cyst, underlining the benefit of anatomical integrity of DW-RARE-EPI.

DISCUSSION

In this study, we demonstrate the feasibility of diffusion-weighted RARE-EPI for ophthalmic DWI free of geometric distortions at 3.0 T and at 7.0 T. Our findings indicate high anatomic integrity for RARE-EPI down to a CAT factor λ = 0.5, meaning that half of the RARE echoes within the echo train are replaced by EPI echoes. Our results demonstrate the anatomic integrity of DW-RARE-EPI for phantoms with distinct structure features as well as for in-vivo ophthalmic imaging. Unlike ss-EPI and rs-EPI no geometric distortions were observed for morphological RARE-EPI phantom imaging. Mean apparent diffusion coefficients derived from RARE-EPI for distilled water accord well with ADCs calculated from diffusion-weighted ss-EPI and rs-EPI. This accordance as well as the agreement with the literature values confirms the correct level of diffusion-sensitization in DW-RARE-EPI. It stands to reason that further reduction in the CAT factor λ can be accomplished by combining RARE-EPI with a PSF encoded strategy for correction of modest distortions evoked by the extension of the EPI echo train [40].

Reduced repetition times and acquisition time shortening were enabled by the reduced RF power deposition in DW-RARE-EPI. Second the SAR advantage of RARE-EPI allowed sequential acquisition of several slices within one TR. Next the SAR economy of DW-RARE-EPI enabled multiband RF pulses for simultaneous multi-slice imaging. In a proof of principle study we showed the feasibility of multiband DW-RARE-EPI of the eye with a multiband factor of 2 and a slice center distance of 1 cm with ample slice separation. The close location of the slices compared to the slice thickness of 5 mm is of particular importance for ophthalmic imaging due to the small size of the eye as the target organ. Due to the RF pulses' low BWTP of 1.15, an overlap of both excited slices is expected. Phantom experiments have been conducted to study the impact on the slice separation and the results reveal a 10% increase in the leakage $L^{99\%}$ from 1.7% to 1.9% when reducing the slice distance from 3 cm to 1 cm. This result and the low leakage values in the in-vivo experiments render the slice distance of 1 cm reasonable. Yet, it is a recognized limitation to our feasibility study that the multiband factor was limited to 2. Replacing the current RF pulses by PINS pulses is a promising candidate to increase the number of simultaneous acquired slices [60-62]. Our approach of applying a combined acquisition technique is compatible with the concept of hyperechoes [63] and variable refocusing flip angles [64] that can serve as measures to further reduce SAR for multiband applications if necessary.

A recognized limitation of the current implementation is the use of 1D linear navigator phase correction to account for unknown phase shifts induced by the diffusion sensitization module within each excitation cycle during the multi-shot acquisition. By this, the diffusion sensitization gradients are limited to the phase encoding axis and the maximum achievable b-value is reduced versus a

scheme exploiting all axes. A 2D linear phase correction [65,66] or a 2D non-linear approach [67] promise to improve the correction robustness and to allow diffusion sensitization gradients along all three axes to increase the achievable maximum b-value. Extending the correction algorithm to a nonlinear algorithm in conjunction with a reacquisition scheme allows further gain in robustness [37]. Navigator correction crosses its borders when motion changes between data and navigator acquisition. To circumvent this, an alternative approach termed multiplexed sensitivity encoding (MUSE) has been suggested [68]. Adding MUSE to our current implementation promises to improve the correction of nonlinear shot-to-shot phase variations. Furthermore, the replacement of the current Cartesian sampling scheme is anticipated. Radial k-space trajectories hold the promise to render additional navigator data unnecessary since the densely sampled k-space center can be deployed for phase correction of motion corrupted data. The use of periodically rotated overlapping parallel lines with enhanced reconstruction (PROPELLER) presents an alternative to fully exploit the benefits of radial k-space sampling for DWI [69]. It is also a recognized limitation of the current implementation, that the acquisition times exceed those of the EPI techniques. However, anatomically correct images free of geometric distortions are obtained as a result of the acquisition time prolongation. Further acceleration in acquisition time can be accomplished by radial undersampling with iterative reconstruction [70] which is compatible to RARE-EPI. Also, the concept of inner volume [71] or ZOOM imaging [72] could be translated to RARE-EPI and thus a further reduction of acquisition times can be achieved.

Further studies with larger sample sizes including volunteers and patients of both sexes are required, but this mandatory precursor was essential before extra variances due to gender and/or pathophysiological conditions are introduced. Extending the current work to a study including patients with intraocular masses is an important step *en route* to the eye clinic.

CONCLUSIONS

To conclude, this study showed that diffusion-weighted RARE-EPI has the capability to acquire ample diffusion contrast, high fidelity, distortion-free images of the eye and the orbit. The results underpin the challenges of ocular imaging at 3.0 T and 7.0 T for echo planar imaging variants and demonstrate that these issues can be offset by using accelerated RARE based approaches. It was shown that RARE-EPI maintains the immunity to B_0 inhomogeneities reported for RARE imaging, which renders RARE-EPI well suited for ophthalmic DWI. This benefit can be exploited for the assessment of spatial arrangements of the eye segments and their masses with the goal to provide guidance in diagnostic assessment and treatment of ophthalmological diseases and neuroophthalmological disorders. These developments may advance the capabilities of MRI based anatomical imaging and tissue characterization at a level of non-invasive interrogation not previously available in humans.

ACKNOWLEDGMENTS

The authors wish to thank Steen Moeller (Department of Radiology and Center for Magnetic Resonance Research, University of Minnesota, Minneapolis, Minnesota, USA) for providing the slice GRAPPA algorithm used for our data analysis. The authors wish to thank Beate Endemann and Andrea Hasselbach (Max-Delbrueck Center for Molecular Medicine in the Helmholtz Association, Berlin, Germany) for their radiological advice.

This work was funded in part (TN) by the Helmholtz Alliance ICEMED – Imaging and Curing Environmental Metabolic Diseases, through the Initiative and Network Fund of the Helmholtz Association.

REFERENCES

1. Mafee MF, et al. Anatomy and Pathology of the Eye: Role of MR Imaging and CT. Neuroimag Clin N Am. 2005;15:23-47.
2. Malhotra A, et al. Ocular Anatomy and Cross-Sectional Imaging of the Eye. Semin Ultrasound CT MR. 2011;32:2-13.
3. Zhang Y, et al. Lamina-Specific Anatomic Magnetic Resonance Imaging of the Human Retina. Invest Ophthalmol Vis Sci. 2011;52:7232-7237.
4. Beenakker J-WM, et al. Automated Retinal Topographic Maps Measured With Magnetic Resonance ImagingRetinal Topographic Maps Measured With MRI. Invest Ophthalmol Vis Sci. 2015;56:1033-1039.
5. Strenk SA, et al. Magnetic resonance imaging of aging, accommodating, phakic, and pseudophakic ciliary muscle diameters. J Cataract Refract Surg. 2006;32:1792-1798.
6. Zhang Y, et al. Blood Flow MRI of the Human Retina/Choroid during Rest and Isometric Exercise. Invest Ophthalmol Vis Sci. 2012;53:4299-4305.
7. Apushkin MA, et al. Retinoblastoma and Simulating Lesions: Role of Imaging. Neuroimag Clin N Am. 2005;15:49-67.
8. de Graaf P, et al. Single-Shot Turbo Spin-Echo Diffusion-Weighted Imaging for Retinoblastoma: Initial Experience. Am J Neuroradiol. 2012;33:110-118.
9. Bolacchi F, et al. Differences between Proximal versus Distal Intraorbital Optic Nerve Diffusion Tensor Magnetic Resonance Imaging Properties in Glaucoma Patients. Invest Ophthalmol Vis Sci. 2012;53:4191-4196.
10. Sepahdari AR, et al. Diffusion-Weighted Imaging of Malignant Ocular Masses: Initial Results and Directions for Further Study. Am J Neuroradiol. 2012;33:314-319.
11. de Graaf P, et al. Guidelines for imaging retinoblastoma: imaging principles and MRI standardization. Pediatr Radiol. 2012;42:2-14.
12. Beenakker JWM, et al. High-resolution MRI of uveal melanoma using a microcoil phased array at 7 T. NMR Biomed. 2013;26:1864-1869.
13. Graessl A, et al. Ophthalmic magnetic resonance imaging at 7 T using a 6-channel transceiver radiofrequency coil array in healthy subjects and patients with intraocular masses. Invest Radiol. 2014;49:260-270.
14. Beenakker JM, et al. Clinical evaluation of ultra-high-field MRI for three-dimensional visualisation of tumour size in uveal melanoma patients, with direct relevance to treatment planning. MAGMA. 2016;doi: 10.1007/s10334-016-0529-4.
15. Clark RA, et al. Magnetic resonance imaging after surgical transposition defines the anteroposterior location of the rectus muscle pulleys. J Pediatr Ophtalmol Strabismus. 1999;3:9-14.
16. Weir RE, et al. The Convex Retina: Optical Coherence Tomography in Hypermetropic Shift, Without Choroidal Folds, from Intraconal Cavernous Haemangioma. Orbit. 2009;28:398-400.
17. Pineles SL, et al. External ophthalmoplegia in human immunodeficiency virus-infected patients receiving antiretroviral therapy. J Pediatr Ophtalmol Strabismus. 2012;16:529-533.
18. Papadopoulou D, et al. How would you manage this small melanocytic choroidal tumour? Br J Ophthalmol. 2012;96:1530-1530.
19. Khurana A, et al. Comparison of the diagnostic value of MR imaging and ophthalmoscopy for the staging of retinoblastoma. Eur Radiol. 2013;23:1271-1280.
20. Lenhart PD, et al. The Role of Magnetic Resonance Imaging in Diagnosing Optic Nerve Hypoplasia. Am J Ophthalmol. 2014;158:1164-1171.e1162.
21. Norris DG, et al. Health and infarcted brain tissues studied at short diffusion times: the origins of apparent restriction and the reduction in apparent diffusion coefficient. NMR Biomed. 1994;7:304-310.
22. Niendorf T, et al. Biexponential diffusion attenuation in various states of brain tissue: Implications for diffusion-weighted imaging. Magn Reson Med. 1996;36:847-857.

23. Bhuta S, et al. Scedosporium apiospermum endophthalmitis: diffusion-weighted imaging in detecting subchoroidal abscess. Clinical Ophthalmology (Auckland, N.Z.). 2012;6:1921-1924.
24. Peeler C, et al. Subretinal abscess causing restricted diffusion on magnetic resonance imaging. J Neuroophthalmol. 2013;33:354-358.
25. Kilicarslan R, et al. Graves' ophthalmopathy: the role of diffusion-weighted imaging in detecting involvement of extraocular muscles in early period of disease. Br J Radiol. 2015;88:20140677.
26. Hiwatashi A, et al. High Resolution Diffusion-Weighted Imaging for Solitary Orbital Tumors : 3D Turbo Field Echo with Diffusion-Sensitized Driven-Equilibrium (DSDE-TFE) Preparation Technique. Clin Neuroradiol. 2017;doi: 10.1007/s00062-016-0556-6.
27. Erb-Eigner K, et al. Diffusion-Weighted Imaging of Ocular Melanoma. Invest Radiol. 2013;48:702-707.
28. He M, et al. The Use of Diffusion MRI in Ischemic Optic Neuropathy and Optic Neuritis. Semin Ophthalmol. 2010;25:225-232.
29. Srinivasan S, et al. Diffusion-weighted MRI in acute posterior ischemic optic neuropathy. Indian Journal of Radiology and Imaging. 2012;22:106-107.
30. Cauquil C, et al. Diffusion MRI and tensor tractography in ischemic optic neuropathy. Acta Neurol Belg. 2012;112:209-211.
31. Meral I, et al. Diffusion changes in the vitreous humor of the eye during aging. AJNR Am J Neuroradiol. 2011;32:1563-1566.
32. Foti PV, et al. Diffusion-weighted magnetic resonance imaging for predicting and detecting the response of ocular melanoma to proton beam therapy: initial results. Radiol Med. 2015;120:526-535.
33. Russo A, et al. Diffusion-weighted magnetic resonance imaging and ultrasound evaluation of choroidal melanomas after proton-beam therapy. Radiol Med. 2015;120:634-640.
34. Xu X, et al. Readout-segmented echo-planar diffusion-weighted imaging in the assessment of orbital tumors: comparison with conventional single-shot echo-planar imaging in image quality and diagnostic performance. Acta Radiol. 2017;doi: 10.1177/0284185117695667:284185117695667.
35. Pipe JG, et al. Multishot diffusion-weighted FSE using PROPELLER MRI. Magn Reson Med. 2002;47:42-52.
36. Robson MD, et al. Diffusion-weighted multiple shot echo planar imaging of humans without navigation. Magn Reson Med. 1997;38:82-88.
37. Porter DA, et al. High resolution diffusion-weighted imaging using readout-segmented echo-planar imaging, parallel imaging and a two-dimensional navigator-based reacquisition. Magn Reson Med. 2009;62:468-475.
38. Heidemann RM, et al. Diffusion imaging in humans at 7T using readout-segmented EPI and GRAPPA. Magn Reson Med. 2010;64:9-14.
39. Paul K, et al. Diffusion-Sensitized Ophthalmic MRI Free of Geometric Distortion at 3.0 T and 7.0 T: A Feasibility Study in Healthy Subjects and Patients with Intraocular Masses. Invest Radiol. 2015;50:309-321.
40. In MH, et al. High-resolution distortion-free diffusion imaging using hybrid spin-warp and echo-planar PSF-encoding approach. Neuroimage. 2017;5:20-30.
41. Norris DG**.** Ultrafast Low-Angle RARE: U-FLARE. Magn Reson Med. 1991;17:539-542.
42. Norris DG, et al. On the application of ultra-fast rare experiments. Magn Reson Med. 1992;27:142-164.
43. Norris DG, et al. Coherence and Interference in Ultrafast RARE Experiments. J Magn Reson. 1993;105:123-127.
44. Hillenbrand C, et al. MR CAT scan: a modular approach for hybrid imaging. MAGMA. 2000;10:183-199.
45. Hillenbrand C, et al. Hybrid cardiac imaging with MR-CAT scan: A feasibility study. J Magn Reson Imaging. 2000;11:711-716.

46. Jakob PM, et al. Abdominal imaging with a modular combination of spin and gradient echoes. Magn Reson Med. 2002;47:425-432.
47. Choli M, et al. Combined acquisition technique (CAT) for high-field neuroimaging with reduced RF power. MAGMA. 2013;26:411-418.
48. Barth M, et al. Simultaneous multislice (SMS) imaging techniques. Magn Reson Med. 2016;75:63-81.
49. Williams CFM, et al. A novel fast split-echo multi-shot diffusion-weighted MRI method using navigator echoes. Magn Reson Med. 1999;41:734-742.
50. Schick F**.** SPLICE: Sub-second diffusion-sensitive MR imaging using a modified fast spin-echo acquisition mode. Magn Reson Med. 1997;38:638-644.
51. Bruder H, et al. Image reconstruction for echo planar imaging with nonequidistant k-space sampling. Magn Reson Med. 1992;23:311-323.
52. Griswold MA, et al. Generalized autocalibrating partially parallel acquisitions (GRAPPA). Magn Reson Med. 2002;47:1202-1210.
53. Park HW, et al. Gradient reversal technique and its applications to chemical-shift-related NMR imaging. Magn Reson Med. 1987;4:526-536.
54. Breuer FA, et al. Controlled aliasing in parallel imaging results in higher acceleration (CAIPIRINHA) for multi-slice imaging. Magn Reson Med. 2005;53:684-691.
55. Hennig J**.** Chemical shift imaging with phase-encoding RF pulses. Magn Reson Med. 1992;25:289-298.
56. Ahmad R, et al. Edge Sharpness Assessment by Parametric Modeling: Application to Magnetic Resonance Imaging. Concepts Magn Reson Part A Bridg Educ Res. 2015;44:138-149.
57. Setsompop K, et al. Blipped-controlled aliasing in parallel imaging for simultaneous multislice echo planar imaging with reduced g-factor penalty. Magn Reson Med. 2012;67:1210-1224.
58. Xu J, et al. Evaluation of slice accelerations using multiband echo planar imaging at 3 T. Neuroimage. 2013;83:991-1001.
59. Schmitter S, et al. Simultaneous multislice imaging in dynamic cardiac MRI at 7T using parallel transmission. Magn Reson Med. 2017;77:1010-1020.
60. Norris DG, et al. Power Independent of Number of Slices (PINS) radiofrequency pulses for low-power simultaneous multislice excitation. Magn Reson Med. 2011;66:1234-1240.
61. Norris DG, et al. Application of PINS radiofrequency pulses to reduce power deposition in RARE/turbo spin echo imaging of the human head. Magn Reson Med. 2014;71:44-49.
62. Gagoski BA, et al. RARE/turbo spin echo imaging with Simultaneous Multislice Wave-CAIPI. Magn Reson Med. 2015;73:929-938.
63. Hennig J, et al. Hyperechoes. Magn Reson Med. 2001;46:6-12.
64. Hennig J, et al. Multiecho sequences with variable refocusing flip angles: optimization of signal behavior using smooth transitions between pseudo steady states (TRAPS). Magn Reson Med. 2003;49:527-535.
65. Butts K, et al. Diffusion-weighted interleaved echo-planar imaging with a pair of orthogonal navigator echoes. Magn Reson Med. 1996;35:763-770.
66. Atkinson D, et al. Sampling and reconstruction effects due to motion in diffusion-weighted interleaved echo planar imaging. Magn Reson Med. 2000;44:101-109.
67. Miller KL, et al. Nonlinear phase correction for navigated diffusion imaging. Magn Reson Med. 2003;50:343-353.
68. Chen NK, et al. A robust multi-shot scan strategy for high-resolution diffusion weighted MRI enabled by multiplexed sensitivity-encoding (MUSE). Neuroimage. 2013;72:41-47.
69. Pipe JG**.** Motion correction with PROPELLER MRI: Application to head motion and free-breathing cardiac imaging. Magn Reson Med. 1999;42:963-969.
70. Merrem A, et al. Rapid Diffusion-Weighted Magnetic Resonance Imaging of the Brain Without Susceptibility Artifacts: Single-Shot STEAM With Radial Undersampling and Iterative Reconstruction. Invest Radiol. 2017;doi: 10.1097/RLI.0000000000000357.

71. Feinberg DA, et al. Inner volume MR imaging: technical concepts and their application. Radiology. 1985;156:743-747.
72. Wheeler-Kingshott CA, et al. ADC mapping of the human optic nerve: increased resolution, coverage, and reliability with CSF-suppressed ZOOM-EPI. Magn Reson Med. 2002;47:24-31.
73. Landolt H, et al. Zahlenwerte und Funktionen aus Physik, Chemie, Astronomie, Geophysik und Technik. 6; Springer-Verlag, 1969.

Table 1

Relaxation parameters of the five compartments in the phantom presented in Figure 3 and 9.

$MnCl_2$ per 1000g H_2O dist.	**3.0 T**			**7.0 T**		
	T_1	**T_2**	**T_2^***	**T_1**	**T_2**	**T_2^***
	(mean ± standard deviation) [ms]					
10 mg (A)	1615 ± 15	219 ± 2	122 ± 37	1557 ± 71	165 ± 3	83 ± 16
20 mg (B)	1108 ± 21	115 ± 4	90 ± 15	1073 ± 90	94 ± 2	52 ± 4
40 mg (C)	697 ± 8	65 ± 2	44 ± 5	647 ± 20	51 ± 4	30 ± 2
70 mg (D)	431 ± 3	35 ± 2	24 ± 2	421 ± 11	33 ± 8	16 ± 1
120 mg (E)	265 ± 5	21 ± 2	15 ± 1	265 ± 2	19 ± 7	10 ± 1

Table 2

Experimental imaging protocols for phantom experiments and in-vivo examinations at 3.0 T and at 7.0 T.

Experiment	Figure	TR [ms]	TE [ms]	ESP [ms]	Receiver bandwidth [Hz/pixel]	Acquisition matrix	FOV [mm^2]	PE direction	Spatial resolution [mm^3]	Acquistion time
Phantom imaging at 3.0 T										
ms-RARE		750	32	6.4	630					15 s per b-value
RARE-EPI		750	32	6.4 (RARE); 2.1 (EPI)	630					15 s per b-value
ss-EPI	3	6200	108	1.3	814	256 x 256	250 x 250	RL	1.0 x 1.0 x 3.0	1:28 min
rs-EPI		200	71	0.4	444					3:00 min
FLASH reference		8.6	4.0		320					
Phantom imaging at 7.0 T										
ms-RARE		1500	31	6.2	630					29 s per b-value
RARE-EPI (λ = 0.7, λ = 0.6, λ = 0.5)		1500	31	6.2 (RARE); 1.9 (EPI)	630					29 s per b-value
ss-EPI	3	3300	115	1.2	1028	256 x 256	250 x 250	RL	1.0 x 1.0 x 3.0	2:47 min
rs-EPI		1000	75	0.3	574					9:59 min
FLASH reference		8.3	3.7		320					
In-vivo brain morphology at 3.0 T										
ms-RARE	5	2000	90	10.0	391	512 x 288 (Partial Fourier; zerofilled to 512 x 384)	188 x 251	RL	0.5 x 0.5 x 3.0	42 s
RARE-EPI (λ = 0.6, λ = 0.5)		2000	90	10.0 (RARE); 2.9 (EPI)	391					
In-vivo brain morphology at 7.0 T										
ms-RARE	5	2000	84	9.3	391	512 x 288 (Partial Fourier; zerofilled to 512 x 384)	251 x 251	RL	0.5 x 0.5 x 3.0	54 s
RARE-EPI (λ = 0.6, λ = 0.5)		2000	84	9.3 (RARE); 2.8 (EPI)	391					
In-vivo ADC mapping at 3.0 T										
ms-RARE			33	6.6	630					20 s per b-value
RARE-EPI (λ = 0.5)			33	6.6 (RARE); 1.9 (EPI)	630					20 s per b-value
ss-EPI	5;11	1000	142	1.4	814	256 x 256	230	RL	0.9 x 0.9 x 5.0	11 s
rs-EPI			81	0.4	444					1:10 min
RARE reference			62	6.6	630					
In-vivo ADC mapping at 7.0 T										
ms-RARE	7	1000	97	10.9	360	512 x 192 (Partial Fourier; zerofilled to 512 x 256)	100 x 200	AP	0.4 x 0.4 x 2.5	23 s per b-value
RARE-EPI (λ = 0.5)		1000	97	10.9 (RARE); 3.2 (EPI)	360					
Morphological multiband imaging at 3.0 T										
ms-RARE	10	2000	34	6.8	630	256 x 256	230	RL	0.9 x 0.9 x 5.0	38 s
RARE-EPI (λ = 0.6)		2000	34	6.8 (RARE); 2.9 (EPI)	630					
Multiband ADC mapping at 3.0 T										
RARE-EPI (λ = 0.6)	12	1000	34	6.8 (RARE); 2.9 (EPI)	630	256 x 256	230	RL	0.9 x 0.9 x 5.0	20 s

Table 3

Mean ADC values determined in an ROI placed within the distilled water compartment in the phantom presented in Figure 3.

	Mean ADC values (± standard deviation) [$\cdot 10^{-3}$ mm^2/s]	
	3.0 T	**7.0 T**
ms-RARE	2.33 ± 0.05	2.09 ± 0.04
RARE-EPI (λ = 0.7)	2.34 ± 0.05	2.20 ± 0.05
RARE-EPI (λ = 0.6)	2.32 ± 0.06	2.20 ± 0.05
RARE-EPI (λ = 0.5)	2.35 ± 0.05	2.21 ± 0.04
ss-EPI	2.19 ± 0.05	2.06 ± 0.04
rs-EPI	2.20 ± 0.03	2.04 ± 0.03
Literature value [73]	2.13 (at 25°C)	

FIGURE LEGENDS

Figure 1

(a) Basic scheme of the diffusion-weighted split-echo RARE-EPI (DW-RARE-EPI) pulse sequence [39,44,49] showing the RF pulse train, the frequency encoding, the slice selection gradients and the phase encoding. Unipolar diffusion sensitization gradients of amplitude G and duration δ are placed along the phase encoding direction and played out prior and after the first refocusing RF pulse. A 1-dimensional navigator signal is acquired for phase correction and motion compensation. The dephasing frequency encoding gradient is imbalanced to split odd and even echoes. The factor λ describes the ratio between RARE echoes and EPI echoes within the echo train. [λ·ETL] RARE echoes are acquired followed by [(1- λ)·ETL] EPI echoes. For better visualization the time scaling is different for the RARE and the EPI part of the echo train. Schematic drawings of the center-out phase encoding scheme **(b)** and the linear scheme which is applied in conjunction with partial Fourier **(c)** are displayed.

Figure 2

Photographs of the applied RF coil setups used in this study. **(a)** A 32-channel head RF coil (Siemens, Erlangen, Germany) used for signal reception in conjunction with a body volume RF coil for signal transmission for phantom and in-vivo studies at 3.0 T. **(b)** For phantom and brain MRI at 7.0 T, a 24-element RF coil array (Nova Medical, Wilmington, USA) was used which is equipped with a quadrature RF volume coil for transmission. **(c)** A dedicated six-element transceiver RF coil array consisting of loop elements was employed together with a TX/RX interface for in-vivo ophthalmic MRI at 7.0 T [13] (MRI.TOOLS GmbH, Berlin, Germany).

Figure 3

(a) Field maps showing the offcenter frequency. Frequency offsets across the measured slices were ΔB_0 = 29.2 Hz at 3.0 T and 56.6 Hz at 7.0 T. **(b)** Images (transaxial slice) of a structure phantom (accommodating 5 cylinders filled with different liquids, d=3.5 cm) acquired at 3.0 T (**left**) and 7.0 T (**right**) using RARE, ss-EPI, rs-EPI and three RARE-EPI variants varying the ratio between RARE and EPI echoes: λ = 0.7 (11 RARE echoes, 5 EPI echoes), λ = 0.6 (10 RARE echoes, 6 EPI echoes), λ = 0.5 (8 RARE echoes, 8 EPI echoes). All images exhibit a spatial resolution of (0.9x0.9x3.0) mm^3. The red contour lines represent the geometry of the FLASH reference image that was acquired with identical geometrical parameters. The red contour was superimposed to all acquisitions to assess the degree of geometric distortions. **(c)** ADC maps masked by the outer contour of the cylindrical phantom are

shown for all six imaging approaches. **(d)** Difference maps were calculated based on the geometrical contours with respect to the FLASH reference image. Mean displacements (± standard deviation) in pixels (px) of the center of gravity of all cylinders are given for each acquisition.

Figure 4

PSF analysis: k-space profiles **(a)** are depicted for RARE (λ = 1) and three RARE-EPI variants with λ = 0.7, λ = 0.6 and λ = 0.5. The part of k-space sampled with RARE echoes is shaded in orange, while the parts filled by EPI echoes are marked in green. **(b)**: The corresponding magnitude of the PSF for each approach is shown. The FWHM of the PSF in pixels (px) is noted as a measure of image quality.

Figure 5

In-vivo images of two healthy subjects acquired at 3.0 T **(a)** and at 7.0 T **(b)** showing a brain slice covering the eyes. Data acquisition was performed with RARE (λ=1; 16 RARE echoes), RARE-EPI (λ=0.6; 10 RARE echoes) and RARE-EPI (λ=0.5; 8 RARE echoes). Magnified views of ROI I covering the eyes (orange), ROI II in the center of the slice (red) and ROI III covering the posterior brain/skull boundary (blue) are shown. The magnified views demonstrate the ability of RARE-EPI to image subtle anatomical brain structures that compare very well with those obtained from RARE imaging. **(c)** Magnified views of the eyes acquired in a different subject demonstrate the effect of the applied phase correction that accounts for differences in phase and temporal position between RARE and EPI echoes. For comparison, an image where the EPI echo lines were substituted by zeros is shown. The spatial resolution is (0.5 x 0.5 x 3.0) mm^3 for all acquisitions.

Figure 6

Comparison of **(a)** anatomical images and **(b)** ADC maps of the eyes calculated from diffusion-weighted data acquired with six b-values ranging from 50 s/mm^2 to 500 s/mm^2 at 3.0 T using RARE (λ = 1), RARE-EPI (λ = 0.5), ss-EPI and rs-EPI. The spatial resolution is (0.9x0.9x5.0) mm^3 for all approaches. **(c)** The ADC maps were masked to show only the eyes and were superimposed to a T_2-weighted RARE image (b=0 s/mm^2) used as anatomical reference. **(d)** Difference maps were calculated based on the geometrical contours of both eye balls with respect to conventional RARE. The mean displacement of the center of gravity of both eye balls is given for RARE-EPI, ss-EPI and rs-EPI. **(e)** ADC maps of the eyes exhibiting a spatial resolution of (0.9x0.9x3.0) mm^3. **(f)** ADC values for pixels within the mask of both eyeballs are plotted for RARE (λ = 1) and RARE-EPI (λ = 0.5). A least-

square fit revealed a linear relation with $y = 1.01 \cdot x$ with a root mean square error (RMSE) of $2.73 \cdot 10^{-4}$ between the two quantities. (g) Bland-Altman-Plot correlating the values presented in (f).

Figure 7

Exemplary results derived from a healthy volunteer at 7.0 T using diffusion-weighted RARE and RARE-EPI ($\lambda = 0.5$). Anatomical images and diffusion-weighted data with b-values of 50 s/mm^2 and 500 s/mm^2 are shown together with the corresponding ADC maps. The difference map of the ADC map acquired using RARE-EPI with $\lambda = 0.5$ with respect to RARE is shown on the right.

Figure 8

(a) Scatter plot summarizing the results of the edge sharpness analysis for all subjects of the feasibility study at 3.0 T and 7.0 T using the eye boundary as profile. The mean is reduced from 0.83 to 0.67 when reducing λ from 1.0 to 0.6. In case multiband imaging was performed both slices were evaluated. (b) Scatter plot summarizing the results of the edge sharpness analysis using the skull boundary as profile. Mean values are 0.87 for $\lambda = 1$ and 0.86 for $\lambda = 0.86$. The differences are non-significant in both cases with a p-value of 0.21 for the analysis using the eye boundary and 0.95 for the skull boundary. (c) Scatter plot summarizing mean ADC values within the vitreous humor of the right and the left eye for the subjects included in the feasibility study. rs-EPI and ss-EPI was performed in only three subjects.

Figure 9

(a) Images (two transaxial slices separated by a gap of 1cm) of the structure phantom acquired at 3.0 T using MB RARE, MB RARE-EPI with $\lambda = 0.6$, ss-EPI and rs-EPI. All images exhibit a spatial resolution of (0.9x0.9x5.0) mm^3. The red contour lines represent the geometry of the FLASH reference image that was acquired with identical geometrical parameters. The red contour was superimposed to all acquisitions to assess the degree of geometric distortions. For RARE and RARE-EPI the aliased MB images are shown on top. Slice 1 and slice 2 were acquired sequentially for ss-EPI and rs-EPI. **(b)** ADC maps masked by the outer contour of the cylindrical phantom are shown for all four imaging approaches. **(c)** Difference maps were calculated based on the geometrical contours with respect to the FLASH reference image. Mean displacements ($\pm$ standard deviation) in pixels (px) of the center of gravity of all cylinders are given for each acquisition.

Figure 10

Aliased and reconstructed MB images acquired at 3.0 T for two slices covering the eyes (location shown in **(a)**) for RARE (λ= 1) and RARE-EPI with λ = 0.7 and λ = 0.6 **(b)**. Corresponding signal leakage maps $L_{1\rightarrow2}$ and $L_{2\rightarrow1}$ in % of the mean vitreous humor signal amplitude are shown in **(c)**.

Figure 11

(a) Aliased MB anatomical images of the eyes for RARE (λ = 1) and RARE-EPI with λ = 0.6. Comparison of **(b)** anatomical images and **(c)** ADC maps of the eyes calculated from diffusion-weighted data acquired with six b-values ranging from 50 s/mm^2 to 500 s/mm^2 at 3.0 T using RARE (λ = 1), RARE-EPI (λ = 0.6), ss-EPI and rs-EPI. The spatial resolution is (0.9x0.9x5.0) mm^3 for all approaches. **(d)** The ADC maps were masked to show only the eyes and were superimposed to a T_2-weighted RARE image (b=0 s/mm^2) used as anatomical reference. **(e)** Difference maps were calculated based on the geometrical contours of both eye balls with respect to conventional RARE. The mean displacement of the center of gravity of both eye balls is given for RARE-EPI, ss-EPI and rs-EPI. For RARE and RARE-EPI un-aliased images are shown for two slices separated by 1 cm. For rs-EPI and ss-EPI the two slices were acquired sequentially.

Figure 12

Diffusion-weighted simultaneous multi-slice images covering the eyes acquired with DW-RARE-EPI (λ = 0.6) at 3.0 T in a healthy volunteer **(a)** and in a subject with an arachnoidal cyst in the left temporal lobe **(b)**. Corresponding ADC maps for both slices are shown on the right. The arachnoidal cyst showed increased ADC values compared to surrounding white and gray matter brain tissue.

Figure 1

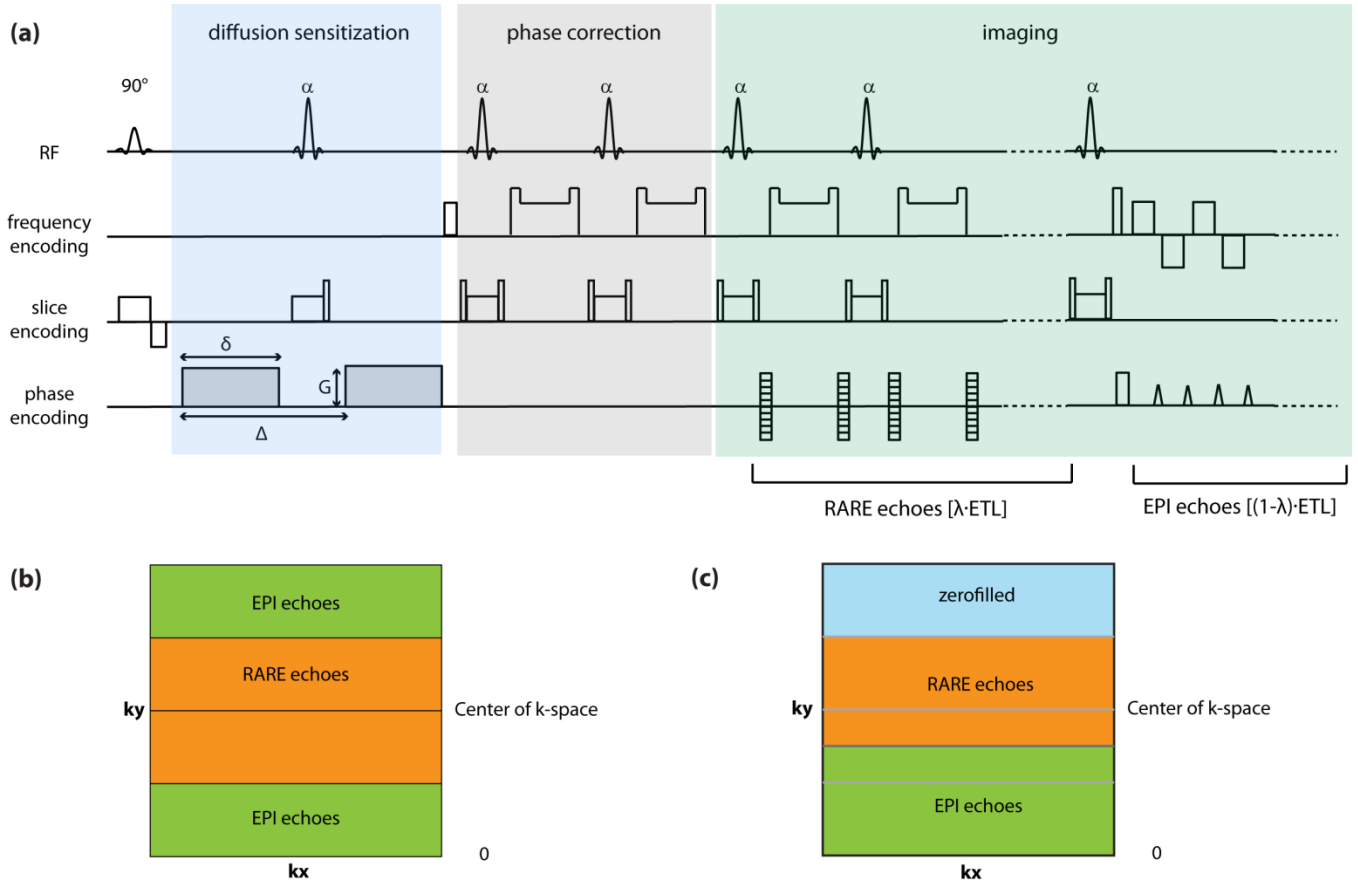
(a)
diffusion sensitization
phase correction
imaging
90°
α
RF
frequency encoding
slice encoding
phase encoding
δ
G
Δ
RARE echoes [λ·ETL]
EPI echoes [(1-λ)·ETL]
(b)
EPI echoes
RARE echoes
ky
Center of k-space
EPI echoes
kx
0
(c)
zerofilled
RARE echoes
ky
Center of k-space
EPI echoes
kx
0

Figure 1:

(a) Basic scheme of the diffusion-weighted split-echo RARE-EPI (DW-RARE-EPI) pulse sequence [38,43,48] showing the RF pulse train, the frequency encoding, the slice selection gradients and the phase encoding. Unipolar diffusion sensitization gradients of amplitude G and duration δ are placed along the phase encoding direction and played out prior and after the first refocusing RF pulse. A 1-dimensional navigator signal is acquired for phase correction and motion compensation. The dephasing frequency encoding gradient is imbalanced to split odd and even echoes. The factor λ describes the ratio between RARE echoes and EPI echoes within the echo train. [λ·ETL] RARE echoes are acquired followed by [(1- λ)·ETL] EPI echoes. For better visualization the time scaling is different for the RARE and the EPI part of the echo train. Schematic drawings of the center-out phase encoding scheme **(b)** and the linear scheme which is applied in conjunction with partial Fourier **(c)** are displayed.

Figure 2

(a) 32-channel head RF coil
3.0 T

(b) 24-channel head RF coil
7.0 T

(c) 6-channel eye coil with TX/RX interface
7.0 T

Figure 2:

Photographs of the applied RF coil setups used in this study. **(a)** A 32-channel head RF coil (Siemens, Erlangen, Germany) used for signal reception in conjunction with a body volume RF coil for signal transmission for phantom and *in-vivo* studies at 3.0 T. **(b)** For phantom and brain MRI at 7.0 T, a 24-element RF coil array (Nova Medical, Wilmington, USA) was used which is equipped with a quadrature RF volume coil for transmission. **(c)** A dedicated six-element transceiver RF coil array consisting of loop elements was employed together with a TX/RX interface for *in-vivo* ophthalmic MRI at 7.0 T [13] (MRI.TOOLS GmbH, Berlin, Germany).

Figure 3

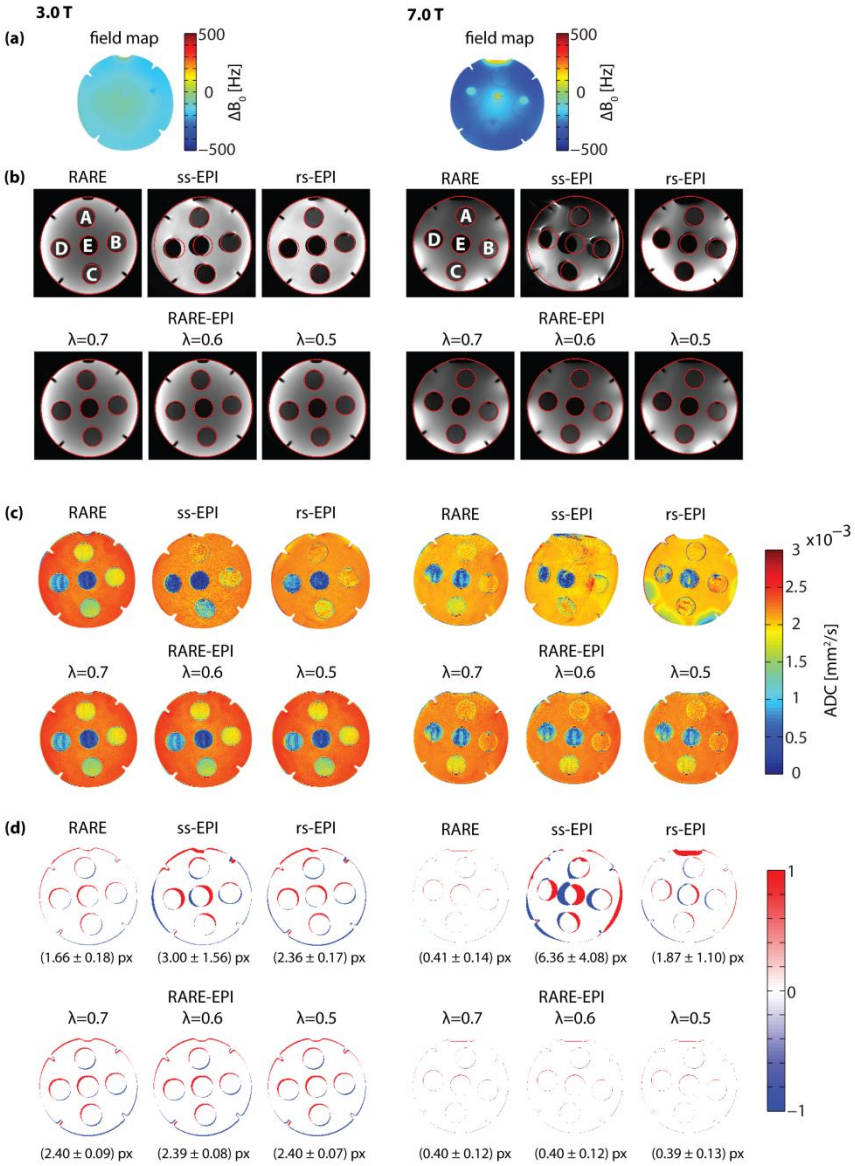
3.0 T
7.0 T
(a)
field map
500
0
−500
ΔB0 [Hz]
(b)
RARE
ss-EPI
rs-EPI
A
B
C
D
E
RARE-EPI
λ=0.7
λ=0.6
λ=0.5
(c)
x10−3
3
2.5
2
1.5
1
0.5
0
ADC [mm²/s]
(d)
(1.66 ± 0.18) px
(3.00 ± 1.56) px
(2.36 ± 0.17) px
(0.41 ± 0.14) px
(6.36 ± 4.08) px
(1.87 ± 1.10) px
(2.40 ± 0.09) px
(2.39 ± 0.08) px
(2.40 ± 0.07) px
(0.40 ± 0.12) px
(0.40 ± 0.12) px
(0.39 ± 0.13) px
1
0
−1

Figure 3:

(a) Images (transaxial slice) of a structure phantom (accommodating 5 cylinders filled with different liquids, d=3.5 cm, the letters A-E refer to the labeling in Table 1) acquired at 3.0 T (**left**) and 7.0 T (**right**) using RARE, ss-EPI, rs-EPI and three RARE-EPI variants varying the ratio between RARE and EPI echoes: $\lambda = 0.7$ (11 RARE echoes, 5 EPI echoes), $\lambda = 0.6$ (10 RARE echoes, 6 EPI echoes), $\lambda = 0.5$ (8 RARE echoes, 8 EPI echoes). All images exhibit a spatial resolution of (0.9x0.9x3.0) mm^3. The red contour lines represent the geometry of the FLASH reference image that was acquired with identical geometrical parameters. The red contour was superimposed to all acquisitions to assess the degree of geometric distortions. **(b)** ADC maps masked by the outer contour of the cylindrical phantom are shown for all six imaging approaches. **(c)** Difference maps were calculated based on the geometrical contours with respect to the FLASH reference image. Mean displacements ($\pm$ standard deviation) in pixels (px) of the center of gravity of all cylinders are given for each acquisition.

Figure 4

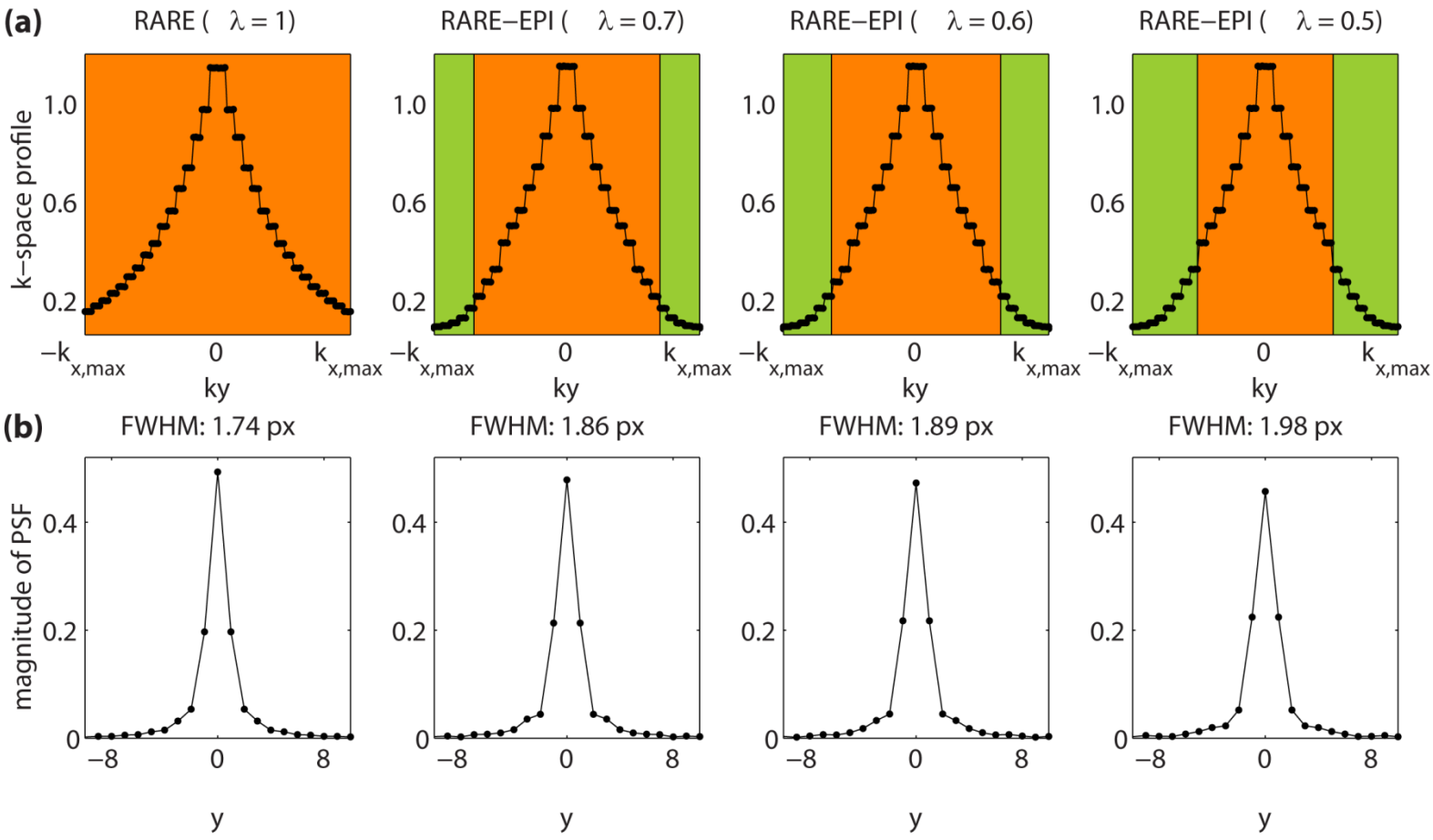
(a)
RARE (λ = 1)
RARE–EPI (λ = 0.7)
RARE–EPI (λ = 0.6)
RARE–EPI (λ = 0.5)
k–space profile
1.0
0.6
0.2
–k x,max
0
k x,max
ky
(b)
FWHM: 1.74 px
FWHM: 1.86 px
FWHM: 1.89 px
FWHM: 1.98 px
magnitude of PSF
0.4
0.2
0
–8
0
8
y

Figure 4:

PSF analysis: k-space profiles **(a)** are depicted for RARE (λ = 1) and three RARE-EPI variants with λ = 0.7, λ = 0.6 and λ = 0.5. The part of k-space sampled with RARE echoes is shaded in orange, while the parts filled by EPI echoes are marked in green. **(b)**: The corresponding magnitude of the PSF for each approach is shown. The FWHM of the PSF in pixels (px) is noted as a measure of image quality.

Figure 5

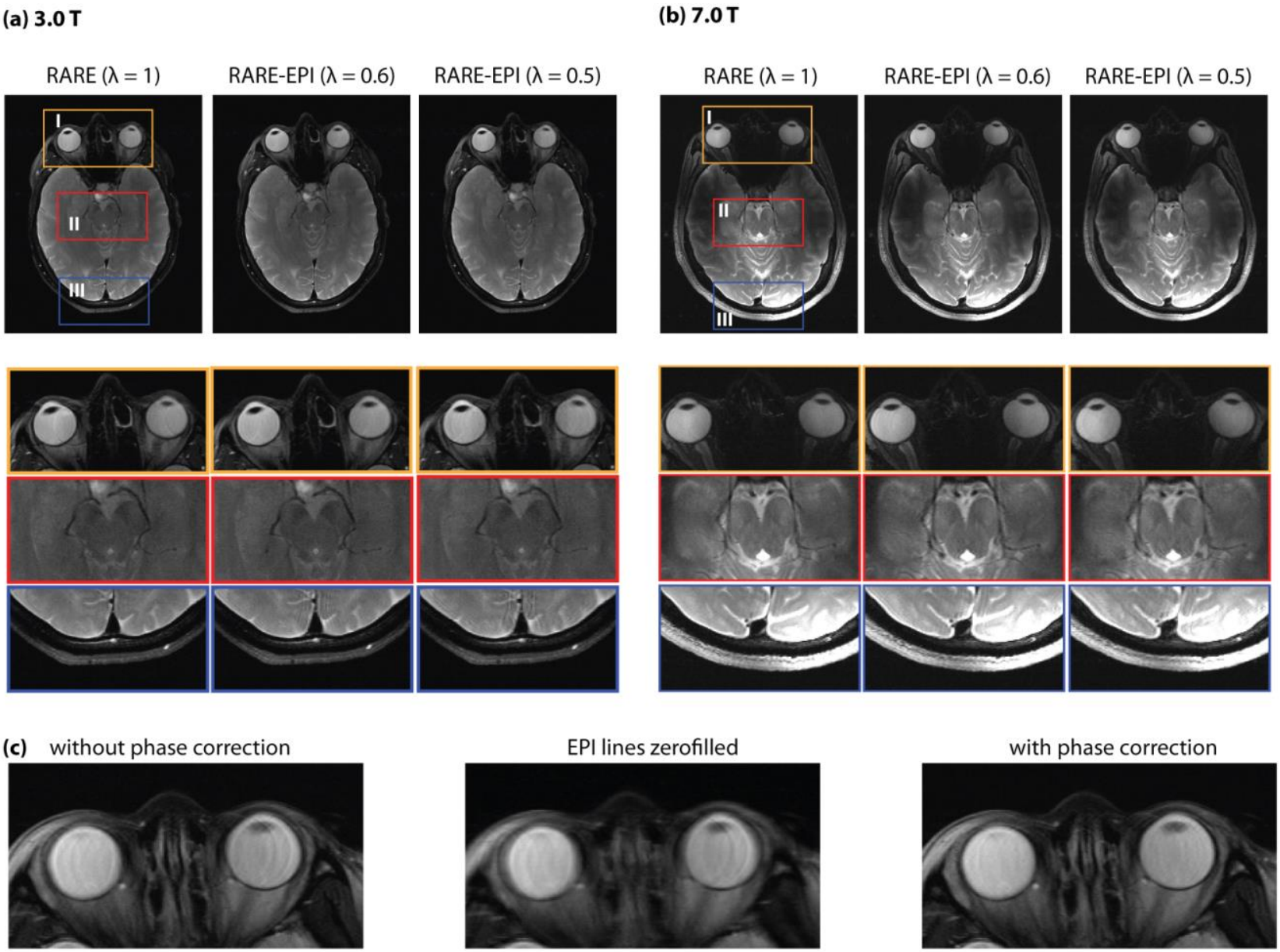
(a) 3.0 T
RARE (λ = 1)
RARE-EPI (λ = 0.6)
RARE-EPI (λ = 0.5)
I
II
III
(b) 7.0 T
RARE (λ = 1)
RARE-EPI (λ = 0.6)
RARE-EPI (λ = 0.5)
I
II
III
(c) without phase correction
EPI lines zerofilled
with phase correction

Figure 5:

In-vivo images of two healthy subjects acquired at 3.0 T **(a)** and at 7.0 T **(b)** showing a brain slice covering the eyes. Data acquisition was performed with RARE (λ=1; 16 RARE echoes), RARE-EPI (λ=0.6; 10 RARE echoes) and RARE-EPI (λ=0.5; 8 RARE echoes). Magnified views of ROI I covering the eyes (orange), ROI II in the center of the slice (red) and ROI III covering the posterior brain/skull boundary (blue) are shown. The magnified views demonstrate the ability of RARE-EPI to image subtle anatomical brain structures that compare very well with those obtained from RARE imaging. **(c)** Magnified views of the eyes acquired in a different subject demonstrate the effect of the applied phase correction that accounts for differences in phase and temporal position between RARE and EPI echoes. For comparison, an image where the EPI echo lines were substituted by zeros is shown. The spatial resolution is (0.5 x 0.5 x 3) mm^3 for all acquisitions.

Figure 6

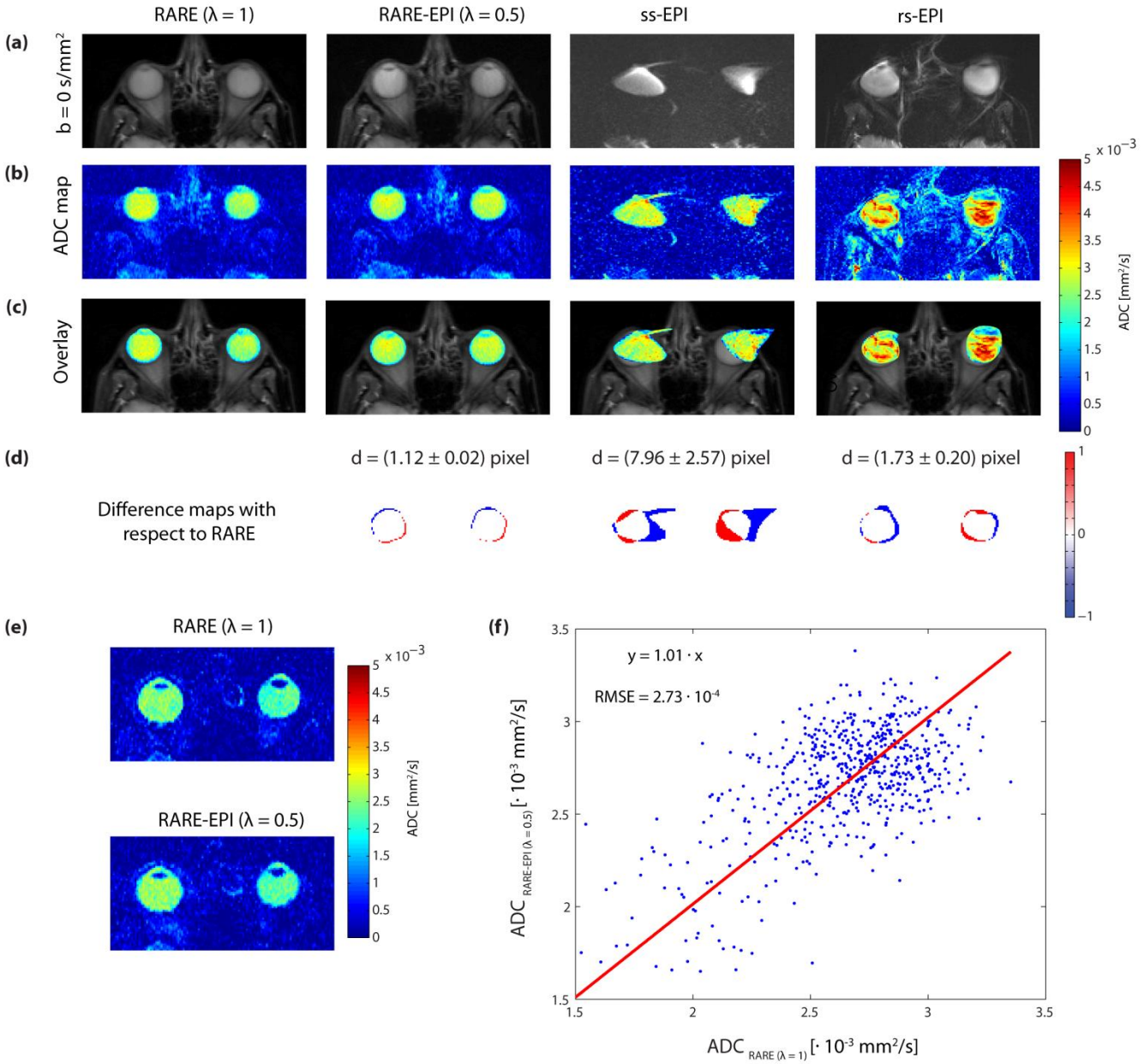
RARE (λ = 1)
RARE-EPI (λ = 0.5)
ss-EPI
rs-EPI
(a)
b = 0 s/mm²
(b)
ADC map
(c)
Overlay
x 10⁻³
5
4.5
4
3.5
3
2.5
2
1.5
1
0.5
0
ADC [mm²/s]
(d)
d = (1.12 ± 0.02) pixel
d = (7.96 ± 2.57) pixel
d = (1.73 ± 0.20) pixel
Difference maps with respect to RARE
1
0
−1
(e)
RARE (λ = 1)
RARE-EPI (λ = 0.5)
x 10⁻³
5
4.5
4
3.5
3
2.5
2
1.5
1
0.5
0
ADC [mm²/s]
(f)
y = 1.01 · x
RMSE = 2.73 · 10⁻⁴
ADC RARE-EPI (λ = 0.5) [· 10⁻³ mm²/s]
ADC RARE (λ = 1) [· 10⁻³ mm²/s]
3.5
3
2.5
2
1.5
1.5
2
2.5
3
3.5

Figure 6:

Comparison of **(a)** anatomical images and **(b)** ADC maps of the eyes calculated from diffusion-sensitized data acquired with six b-values ranging from 50 s/mm^2 to 500 s/mm^2 at 3.0 T using RARE (λ = 1), RARE-EPI (λ = 0.5), ss-EPI and rs-EPI. The spatial resolution is (0.9x0.9x5.0) mm^3 for all approaches. **(c)** The ADC maps were masked to show only the eyes and were superimposed to a T_2-weighted RARE image (b=0 s/mm^2) used as anatomical reference. **(d)** Difference maps were calculated with respect to conventional RARE. The mean displacement of the center of gravity of both eye balls is given for RARE-EPI, ss-EPI and rs-EPI. **(e)** ADC maps of the eyes exhibiting a spatial resolution of (0.9x0.9x3.0) mm^3. **(f)** ADC values within the mask of both eyeballs are plotted for RARE (λ = 1) and RARE-EPI (λ = 0.5). A least-square fit revealed a linear relation with $y = 1.01 \cdot x$ with a root mean square error (RMSE) of $2.73 \cdot 10^{-4}$ between the two quantities. (g) Bland-Altman-Plot correlating the values presented in (f).

Figure 7

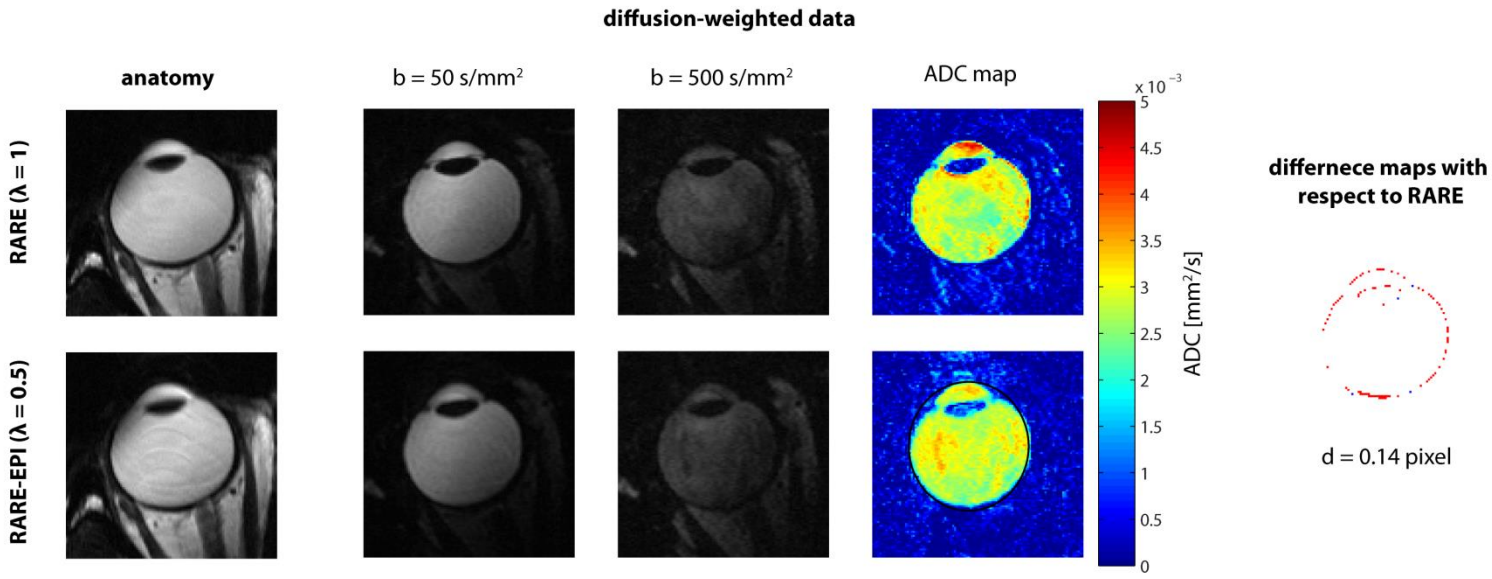
diffusion-weighted data
anatomy
b = 50 s/mm²
b = 500 s/mm²
ADC map
RARE (λ = 1)
RARE-EPI (λ = 0.5)
x 10⁻³
5
4.5
4
3.5
3
2.5
2
1.5
1
0.5
0
ADC [mm²/s]
differnece maps with respect to RARE
d = 0.14 pixel

Figure 7:

Exemplary results derived from two healthy volunteers at 7.0 T using diffusion-weighted RARE and RARE-EPI ($\lambda = 0.5$). Anatomical images and diffusion-weighted data with b-values of 50 s/mm^2 and 500 s/mm^2 are shown together with the corresponding ADC maps. The difference map of the ADC map acquired using RARE-EPI with $\lambda = 0.5$ with respect to RARE is shown on the right.

Figure 8

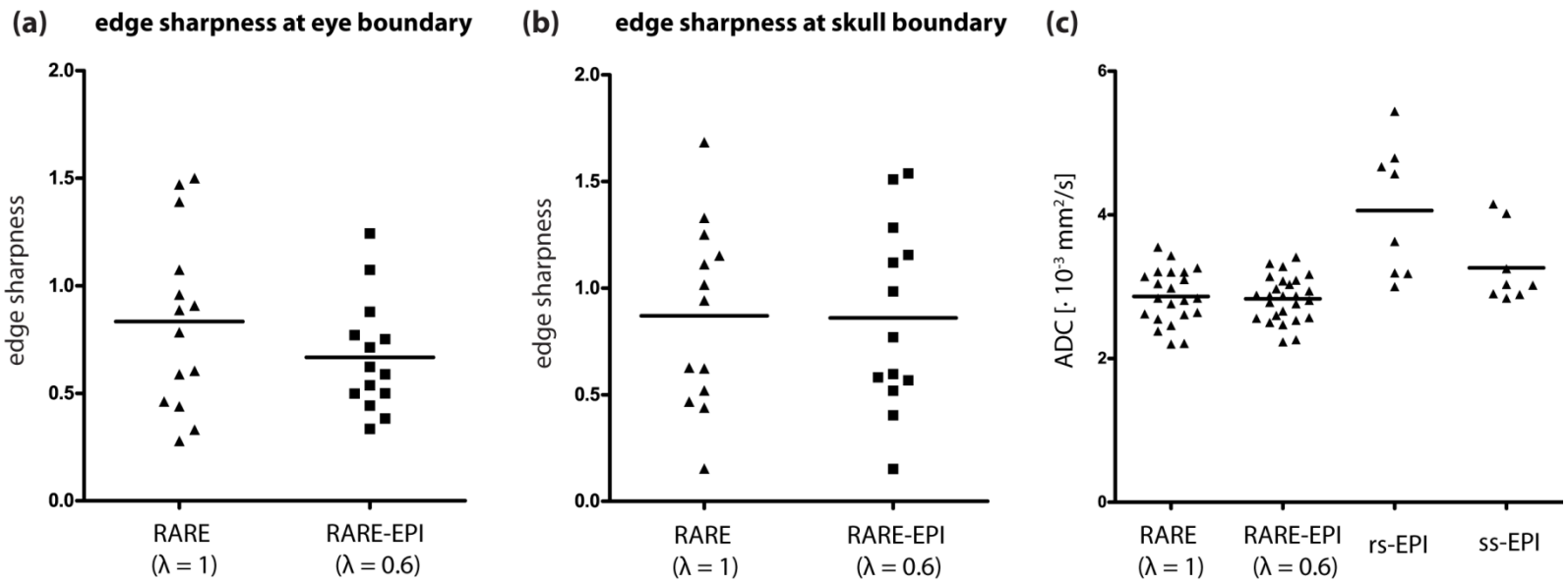
(a)
edge sharpness at eye boundary
edge sharpness
2.0
1.5
1.0
0.5
0.0
RARE
(λ = 1)
RARE-EPI
(λ = 0.6)
(b)
edge sharpness at skull boundary
edge sharpness
2.0
1.5
1.0
0.5
0.0
RARE
(λ = 1)
RARE-EPI
(λ = 0.6)
(c)
ADC [· 10⁻³ mm²/s]
6
4
2
0
RARE
(λ = 1)
RARE-EPI
(λ = 0.6)
rs-EPI
ss-EPI

Figure 8:

(a) Scatter plot summarizing the results of the edge sharpness analysis for all subjects of the feasibility study at 3.0 T and 7.0 T using the eye boundary as profile. The mean is reduced from 0.83 to 0.67 when reducing λ from 1.0 to 0.6. In case multiband imaging was performed both slices were evaluated. (b) Scatter plot summarizing the results of the edge sharpness analysis using the skull boundary as profile. Mean values are 0.87 for λ = 1 and 0.86 for λ = 0.86. The differences are non-significant in both cases with a p-value of 0.21 for the analysis using the eye boundary and 0.95 for the skull boundary. (c) Scatter plot summarizing mean ADC values within the vitreous humor of the right and the left eye for the subjects included in the feasibility study. rs-EPI and ss-EPI was performed in only three subjects.

Figure 9

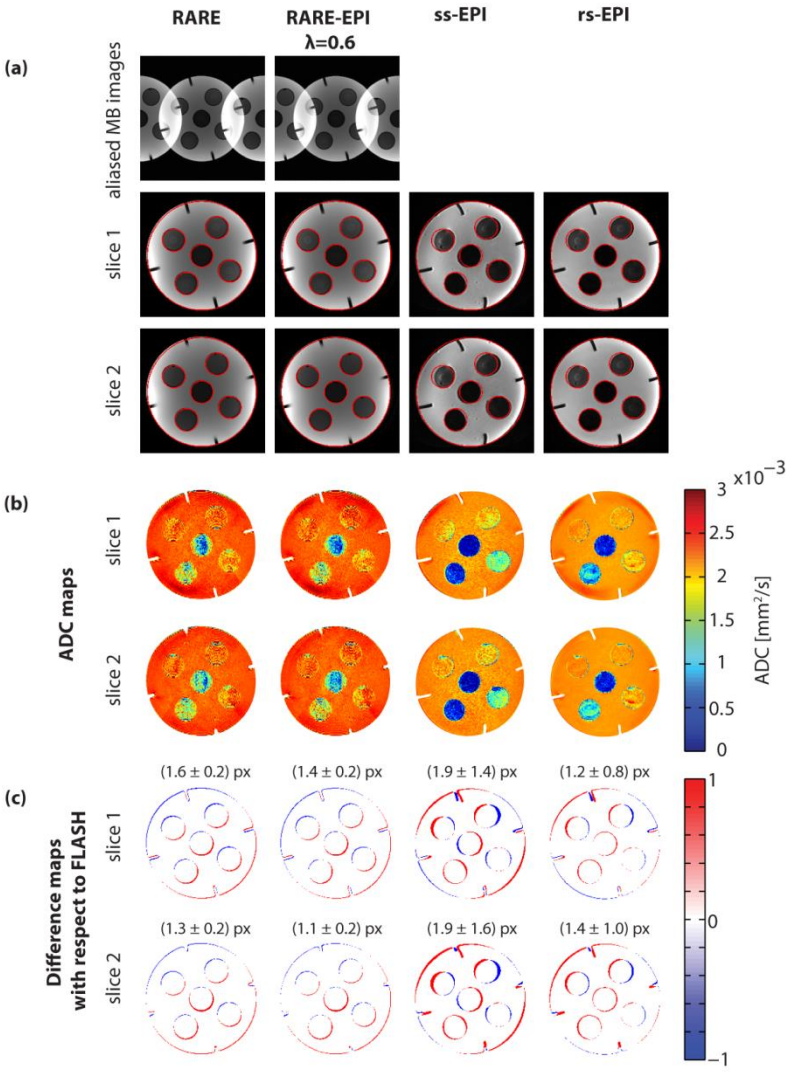
RARE
RARE-EPI
λ=0.6
ss-EPI
rs-EPI
(a)
aliased MB images
slice 1
slice 2
(b)
ADC maps
slice 1
slice 2
x10−3
3
2.5
2
1.5
1
0.5
0
ADC [mm²/s]
(c)
Difference maps
with respect to FLASH
slice 1
slice 2
(1.6 ± 0.2) px
(1.4 ± 0.2) px
(1.9 ± 1.4) px
(1.2 ± 0.8) px
(1.3 ± 0.2) px
(1.1 ± 0.2) px
(1.9 ± 1.6) px
(1.4 ± 1.0) px
1
0
−1

Figure 9:

(a) Images (two transaxial slices separated by a gap of 1cm) of the structure phantom acquired at 3.0 T using MB RARE, MB RARE-EPI with $\lambda = 0.6$, ss-EPI and rs-EPI. All images exhibit a spatial resolution of (0.9x0.9x5.0) mm^3. The red contour lines represent the geometry of the FLASH reference image that was acquired with identical geometrical parameters. The red contour was superimposed to all acquisitions to assess the degree of geometric distortions. For RARE and RARE-EPI the aliased MB images are shown on top. Slice 1 and slice 2 were acquired sequentially for ss-EPI and rs-EPI. **(b)** ADC maps masked by the outer contour of the cylindrical phantom are shown for all four imaging approaches. **(c)** Difference maps were calculated based on the geometrical contours with respect to the FLASH reference image. Mean displacements ($\pm$ standard deviation) in pixels (px) of the center of gravity of all cylinders are given for each acquisition.

Figure 10

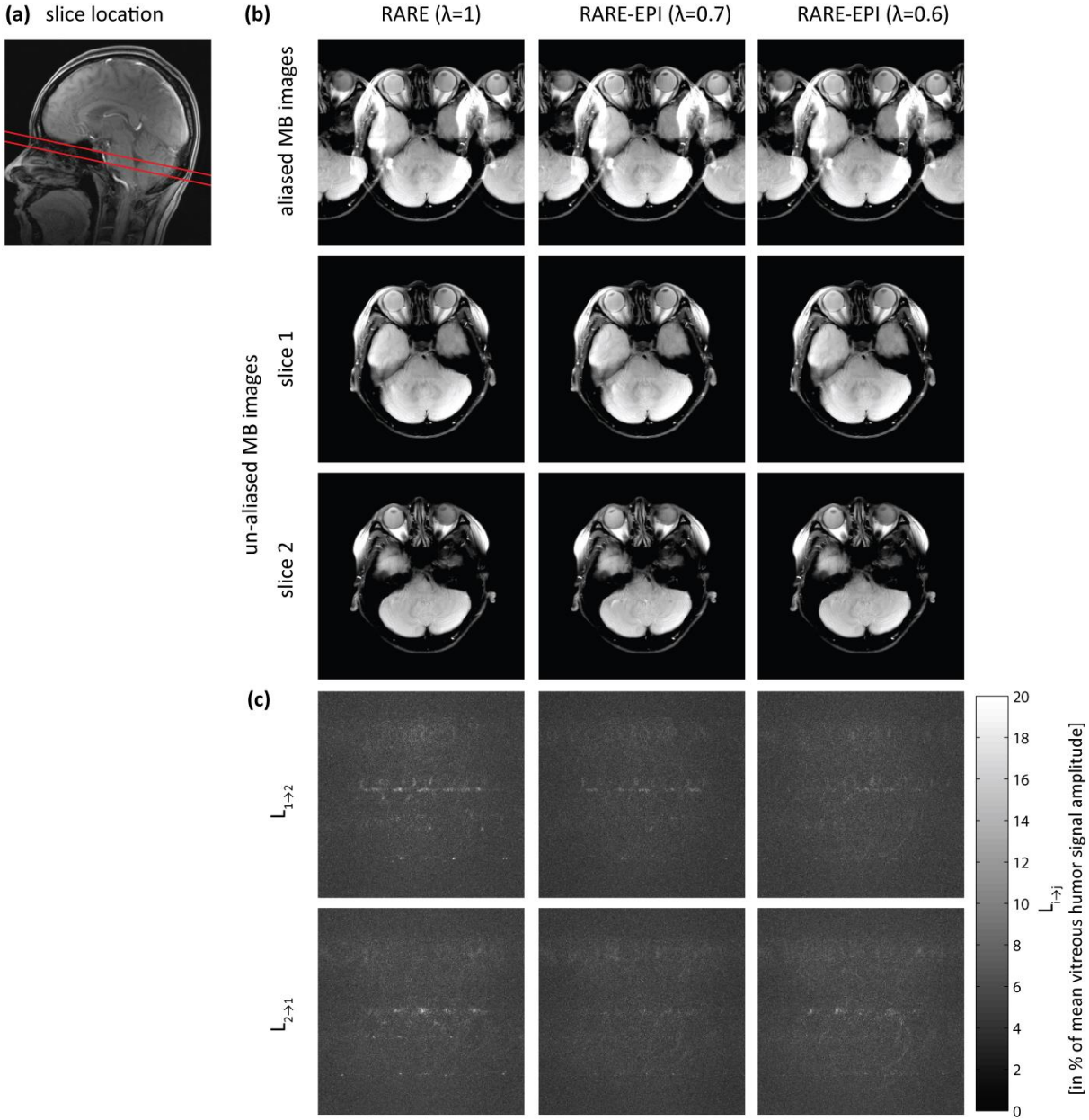
(a) slice location
(b)
RARE (λ=1)
RARE-EPI (λ=0.7)
RARE-EPI (λ=0.6)
aliased MB images
un-aliased MB images
slice 1
slice 2
(c)
$L_{1\to2}$
$L_{2\to1}$
20
18
16
14
12
10
8
6
4
2
0
$L_{i\to j}$
[in % of mean vitreous humor signal amplitude]

Figure 10:

Aliased and reconstructed MB images acquired at 3.0 T for two slices covering the eyes (location shown in **(a)**) for RARE (λ= 1) and RARE-EPI with λ = 0.7 and λ = 0.6 **(b)**. Corresponding signal leakage maps $L_{1\rightarrow 2}$ and $L_{2\rightarrow 1}$ in % of the mean vitreous humor signal amplitude are shown in **(c)**.

Figure 11

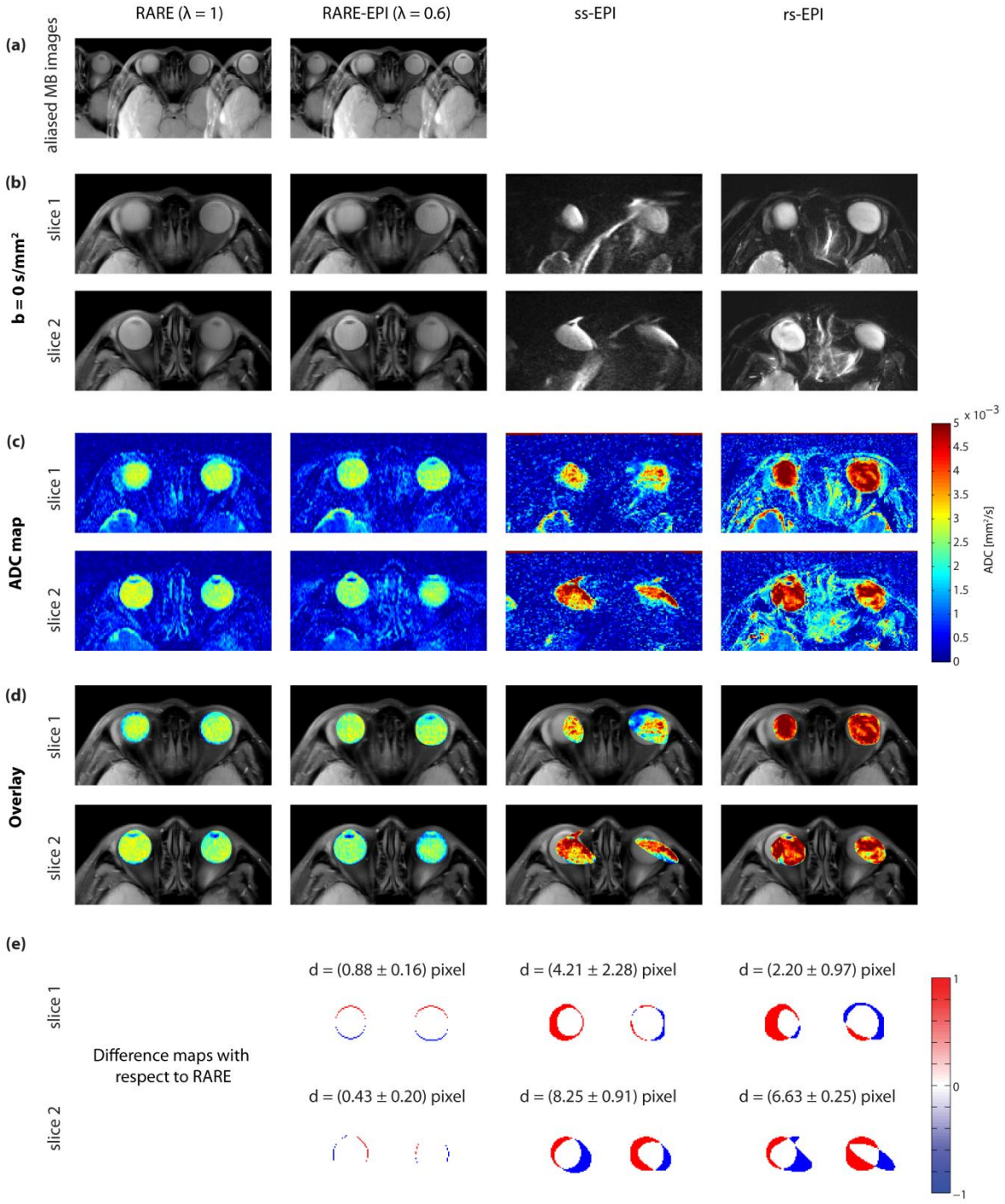
RARE (λ = 1)
RARE-EPI (λ = 0.6)
ss-EPI
rs-EPI
(a)
aliased MB images
(b)
b = 0 s/mm²
slice 1
slice 2
(c)
ADC map
slice 1
slice 2
x 10⁻³
5
4.5
4
3.5
3
2.5
2
1.5
1
0.5
0
ADC [mm²/s]
(d)
Overlay
slice 1
slice 2
(e)
slice 1
slice 2
Difference maps with respect to RARE
d = (0.88 ± 0.16) pixel
d = (4.21 ± 2.28) pixel
d = (2.20 ± 0.97) pixel
d = (0.43 ± 0.20) pixel
d = (8.25 ± 0.91) pixel
d = (6.63 ± 0.25) pixel
1
0
−1

Figure 11:

(a) Aliased MB anatomical images of the eyes for RARE (λ = 1) and RARE-EPI with λ = 0.6. Comparison of **(b)** anatomical images and **(c)** ADC maps of the eyes calculated from diffusion-weighted data acquired with six b-values ranging from 50 s/mm^2 to 500 s/mm^2 at 3.0 T using RARE (λ = 1), RARE-EPI (λ = 0.6), ss-EPI and rs-EPI. The spatial resolution is (0.9x0.9x5.0) mm^3 for all approaches. **(d)** The ADC maps were masked to show only the eyes and were superimposed to a T_2-weighted RARE image (b=0 s/mm^2) used as anatomical reference. **(e)** Difference maps were calculated based on the geometrical contours of both eye balls with respect to conventional RARE. The mean displacement of the center of gravity of both eye balls is given for RARE-EPI, ss-EPI and rs-EPI. For RARE and RARE-EPI un-aliased images are shown for two slices separated by 1 cm. For rs-EPI and ss-EPI the two slices were acquired sequentially.

Figure 12

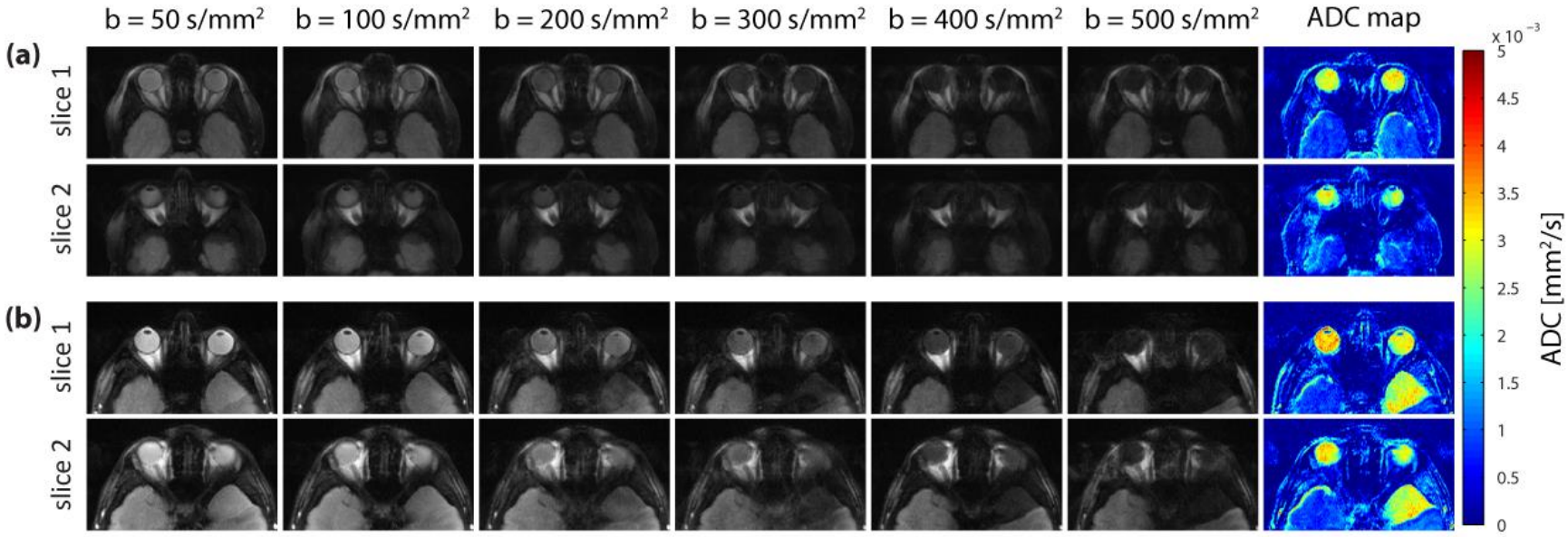
b = 50 s/mm²
b = 100 s/mm²
b = 200 s/mm²
b = 300 s/mm²
b = 400 s/mm²
b = 500 s/mm²
ADC map
(a)
slice 1
slice 2
(b)
slice 1
slice 2
x 10⁻³
5
4.5
4
3.5
3
2.5
2
1.5
1
0.5
0
ADC [mm²/s]

Figure 12:

Diffusion-weighted simultaneous multi-slice images covering the eyes acquired with DW-RARE-EPI (λ = 0.6) at 3.0 T in a healthy volunteer **(a)** and in a volunteer with an incidental finding of an arachnoidal cyst in the left temporal lobe **(b)**. Corresponding ADC maps for both slices are shown on the right. The arachnoidal cyst showed increased ADC values compared to surrounding white and gray matter brain tissue.